Featured in Physics

In Situ Magnetometry of Iron in Human Dopaminergic Neurons Using Superresolution MRI and Ion-Beam Microscopy

Malte Brammerloh,[1–3,†] Renat Sibgatulin,[4] Karl-Heinz Herrmann,[4] Markus Morawski,[1,5] Tilo Reinert,[1,5] Carsten Jäger,[1,5] Roland Müller,[1] Gerald Falkenberg,[6] Dennis Brückner,[6] Kerrin J. Pine,[1] Andreas Deistung,[7] Valerij G. Kiselev,[8] Jürgen R. Reichenbach,[4] Nikolaus Weiskopf,[1,3,9,*] and Evgeniya Kirilina[1,*]

[1]*Department of Neurophysics, Max Planck Institute for Human Cognitive and Brain Sciences, Stephanstrasse 1a, 04103 Leipzig, Germany*
[2]*International Max Planck Research School on Neuroscience of Communication: Function, Structure, and Plasticity*
[3]*Felix Bloch Institute for Solid State Physics, Faculty of Physics and Earth System Sciences, Leipzig University, Linnéstrasse 5, 04103 Leipzig, Germany*
[4]*Medical Physics Group, Institute of Diagnostic and Interventional Radiology, Jena University Hospital, Philosophenweg 3, 07743 Jena, Germany*
[5]*Paul Flechsig Institute—Centre of Neuropathology and Brain Research, Leipzig University, Liebigstrasse 19, 04103 Leipzig, Germany*
[6]*Deutsches Elektronen-Synchrotron DESY, Notkestrasse 85, 22607 Hamburg, Germany*
[7]*University Clinic and Outpatient Clinic for Radiology, University Hospital Halle (Saale), University Medicine Halle, Ernst-Grube-Strasse 40, 06120 Halle (Saale), Germany*
[8]*Division of Medical Physics, Department of Diagnostic and Interventional Radiology, University Medical Center Freiburg, Faculty of Medicine, University of Freiburg, Freiburg, Germany*
[9]*Wellcome Centre for Human Neuroimaging, Institute of Neurology, University College London, 12 Queen Square, London WC1N 3AR, United Kingdom*

(Received 30 May 2023; revised 18 January 2024; accepted 27 March 2024; published 10 June 2024)

Paramagnetic transition metals play a crucial role as cofactors in various cellular catalytic processes. However, their high concentrations in reactive oxidation states can induce oxidative stress, resulting in cell dysfunction or death. Hence, it is vital to have methods to monitor metal concentrations and paramagnetic properties in cells for medicine and cell biology. Here we present a novel multimodal method for in-cell magnetometry enabling direct measurement of metal magnetic properties within individual cells in tissue, without prior isolation and at room temperature. Individual cell magnetic moments are measured using superresolution magnetic resonance imaging (MRI) microscopy at 9.4 T by detecting microscopic magnetic-field perturbations around the cells. The cellular metal content is quantified using ion-beam microscopy or synchrotron micro-x-ray fluorescence for the same cells. The metal magnetic susceptibility at 9.4 T is then obtained from the slope of the cell magnetic moments' dependence on cell metal content. To estimate the susceptibility at lower fields, multifield MR relaxometry and biophysical modeling are employed, extrapolating the 9.4-T susceptibility values to fields as low as 3 T. We apply the new method to determine the susceptibility of iron accumulated in human dopaminergic neurons inside neuromelanin, the by-product of dopamine synthesis. The susceptibility of iron in neuromelanin is measured to be $\chi_\rho = (2.98 \pm 0.19) \times 10^{-6}$ m^3/kg providing unique insights into the biochemistry of iron inside dopaminergic neurons. The obtained value reveals a predominant monoatomic low-affinity iron-binding site within neuromelanin, indicating a higher neurotoxicity of iron than previously suggested. Furthermore, the measured susceptibility value establishes a quantitative relationship between cellular iron concentration and iron-sensitive MRI parameters, which can be noninvasively measured *in vivo*. This breakthrough paves the way for the *in vivo* detection of dopaminergic neuron density and iron load, requiring a standard clinical MRI scanner only. It promises to facilitate early diagnosis of Parkinson's disease. In conclusion, our presented novel

*These authors contributed equally to this work.
†mbrammerloh@cbs.mpg.de

method enables the direct measurements of magnetic properties of paramagnetic metals within single cells with high sensitivity and across large cell groups within a macroscopic volume, providing invaluable information about the cellular biology of metals.

DOI: 10.1103/PhysRevX.14.021041

Subject Areas: Biological Physics, Interdisciplinary Physics, Magnetism, Medical Physics

I. INTRODUCTION

Paramagnetic transition metals play crucial roles in a variety of cellular processes, serving as essential cofactors for enzymes involved in energy metabolism, DNA synthesis, and antioxidant defense [1]. Some cell types in the human body accumulate particularly high levels of transition metals, which they need for their specific functions. For instance, dopaminergic neurons in the substantia nigra store iron, which is required for dopamine synthesis [2]. Hepatocytes in the liver take up iron, copper, and zinc, regulating their systemic levels [3], while prostate cells accumulate zinc, which is essential for their function [4]. However, when present in high concentrations or certain reactive oxidation states, iron, and other paramagnetic transition metals can induce oxidative stress, leading to cellular dysfunction or even cell death. Thus, measuring the cellular concentrations and paramagnetic properties of these metals is of great importance for both basic cell biology and clinical research. In recent years, magnetic resonance imaging (MRI) has emerged as a powerful tool for noninvasively measuring tissue concentrations of paramagnetic metals, including iron. However, conventional MRI does not provide sufficient resolution to resolve individual cells or cell populations.

Herein, we present a new technique for in-cell magnetometry that allows direct measurement of the paramagnetic properties of metals within individual cells without the need for unphysiological metal extraction from the cell and cell isolation from the tissue. The method combines ultra-high-field and superresolution MRI microscopy on postmortem tissue, biophysical modeling, and cellular metal quantification using proton-induced x-ray emission (PIXE) and synchrotron micro-x-ray fluorescence imaging (XRF) (Fig. 1). The method allows single-cell detection with high absolute sensitivity at room temperature and in fully hydrated tissue. At the same time, it provides macroscopic coverage, imaging thousands of cells in a single experiment.

We demonstrate the performance of the method in an important neuroscientific application. We measure the magnetic susceptibility of iron in dopaminergic neurons within the human brain. The obtained value offers valuable contributions to understanding the biochemistry of iron within these critical cells. By determining the prevailing form of iron binding in the biopolymer neuromelanin within dopaminergic neurons, we shed light on the potential higher toxicity of iron within dopaminergic neurons than previously assumed. Furthermore, the determined susceptibility values and developed biophysical model establish a crucial quantitative link between clinical macroscopic MRI markers of brain iron and microscopic cellular iron loads, offering a valuable bridge for radiologists and neuroscientists. This breakthrough may enable the *in vivo* detection of dopaminergic neuron loss, thereby opening new possibilities for early diagnosis of Parkinson's disease.

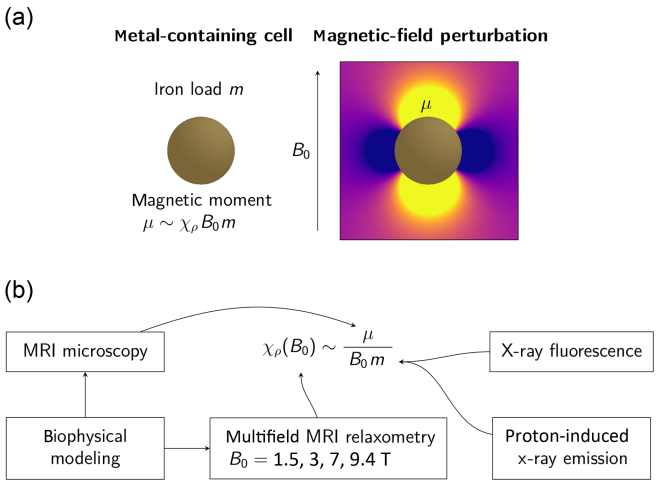

FIG. 1. Overview of the proposed multimodal method for in-cell magnetometry. (a) A cell containing a total mass m of paramagnetic metal is placed in a magnetic field B_0 of the MRI scanner. The metal is magnetized, and the cell gets a magnetic moment μ. The magnetized cell perturbs the magnetic field around it, and the perturbations are proportional to the product of m, B_0, and the mass magnetic susceptibility of the metal χ_ρ at B_0. (b) χ_ρ is determined by a combination of MRI microscopy, MRI relaxometry, and advanced methods for metal quantification (PIXE and XRF). In the first step, χ_ρ is measured at an ultrahigh field of 9.4 T. For this purpose, the magnetic moments of individual cells are measured by MRI microscopy on tissue samples by detecting local field perturbations around the cells. XRF and PIXE measure the cellular iron content of the same cells. These two measurements determined χ_ρ at ultrahigh field. In the next step, the χ_ρ value obtained at ultrahigh field is extrapolated to lower field strengths using MRI relaxometry at different field strengths. The interpretation of MRI microscopy and MRI relaxometry are based on a biophysical model of metal-induced MRI contrast.

A. Iron in dopaminergic neurons

Dopaminergic neurons (DNs) in the substantia nigra pars compacta (SNpc) in the midbrain play a pivotal role in the healthy and diseased human brain. In these neurons, the neurotransmitter dopamine is synthesized, which contributes critically to the regulation of motor and reward behaviors [5,6]. Most prominently, DN depletion is the central hallmark of Parkinson's disease (PD) [7]. Currently, it is only possible to diagnose PD after the majority of DNs in the SNpc are already depleted [8]. Novel treatment approaches of PD aim to halt or slow the DN depletion [9]. Hence, methods to quantify surrogates of dopaminergic function *in vivo* would be highly desirable for neuroscience, clinical diagnostics, and treatment monitoring.

Dopamine synthesis in DN depends on iron, which serves as a cofactor in the enzyme tyrosine hydroxylase. Therefore, DNs store high levels of paramagnetic iron in the pigment neuromelanin (NM), which accumulates in the neuron bodies, or somata, as a by-product of dopamine synthesis over the lifespan [2,10,11].

NM may play a protective or harmful role depending on the chemical iron-binding form, which also determines the magnetic properties of iron. Electron paramagnetic resonance and magnetometry using a superconducting quantum interference device (SQUID) on NM extracted from postmortem tissue suggested that iron in NM is stored in two binding sites with different biological activity and different magnetic properties: a mononuclear, low-affinity binding site of paramagnetic iron (Fe^{3+}) ions with electron spin $5/2$ and a crystalline, high-affinity binding site of iron ions coordinated in a ferrihydrite crystal as Fe^{3+} to iron in iron-storage protein ferritin [9,11,12]. The spins of iron ions bound to the crystalline site in grains of variable size are coupled antiferromagnetically [12]. Uncompensated spins on the surface of these grains align in parallel, giving rise to a net magnetic moment that shows superparamagnetic behavior [12]. In health, neuromelanin's high-affinity binding site acts neuroprotective, as herein iron is redox inactive, preventing neurotoxicity via Fenton chemistry [13]. The low-affinity iron-binding site may act neurotoxic, as herein iron easily leaks out of NM. Iron overload in NM, for instance, in PD [2], may saturate the high-affinity binding site [14] increasing levels of neurotoxic mononuclear iron, potentially causing DN depletion.

The two iron-binding sites in NM exhibit distinct magnetic properties. In extracted NM, the mononuclear binding site is occupied by a paramagnetic iron ion with the electron spin $5/2$, and its magnetism is described by Curie's law. The crystalline binding site hosts iron grains similar to those of iron-binding protein ferritin. The grains are formed by multiple iron atoms coupled by oxyhydroxy bridges and show superparamagnetic behavior [11,12]. Hence, the magnetometry of NM offers a rare glimpse into the physiological role of iron, as distinct magnetic properties are expected for iron in the neuroprotective and neurotoxic binding sites in NM. Ideally, the magnetometry should be performed directly inside the cells without prior extraction since the NM extraction procedure alters the iron distribution between the two binding sites [15].

B. MRI for iron quantification

Recent advances in MRI bring *in vivo* quantification of dopaminergic neurons [16,17] into reach. MRI is sensitive to DN due to paramagnetic iron in NM, which impacts several MRI parameters, including longitudinal [18], transverse, and effective transverse relaxation rates [10,19,20], magnetic susceptibility [21], and the image intensity in MRI sequences sensitive to NM [22] most probably via magnetization transfer effects. Especially promising are approaches based on NM-sensitive MRI [23] and on transverse and effective transverse relaxation rates R_2 and R_2^* [10,19,24]. While results show the great potential of MRI-based biomarkers of dopaminergic neurons, no quantitative biomarker of DNs is available to date. Developing a quantitative MRI-based biomarker of DNs requires a profound understanding of the magnetic properties of neuromelanin. MRI quantitative susceptibility mapping (QSM) [25] offers an avenue toward studying the magnetism of NM in tissue, overcoming the limitation of studies of extracted NM [10,19]. Usually, QSM is used to study the magnetic susceptibility of brain regions encompassing several MRI voxels on the millimeter length scale [26]. QSM has been successfully applied to study brain iron alterations in aging [27–29] and pathologies such as PD [30,31]. However, the typical MRI resolution far exceeds the dimensions of the NM clusters inside of dopaminergic neurons, approximately 10 μm, whose susceptibility we aim to quantify [32]. MRI microscopy on postmortem tissue at ultrahigh magnetic-field strengths (>7 T) offers increased resolution of 20 to 50 μm [33–35]. In this case, an NM cluster only partly occupies one or few neighboring MRI voxels, and this partial volume effect complicates the quantification of the cluster's susceptibility.

We have recently shown [10] that the relaxation due to NM clusters is well described by static dephasing theory [36]. In this regime, the effective transverse relaxation rate R_2^* carries information about the magnetic moment of NM clusters.

C. MRI microscopy for in-cell magnetometry

Here we demonstrate that MRI microscopy resolves individual NM-rich DN cell bodies (somata) and provides 3D cellular maps of the entire SN. We characterized the magnetic properties of individual neurons by determining the magnetic susceptibility of iron in neuromelanin. We quantified the susceptibility of NM-bound iron within DNs, using a superresolution QSM approach with MRI voxel sizes close to the size of single cells and employing biophysical modeling of the MRI signal. We indirectly examined the dependence of that susceptibility value on the

static magnetic-field strength between 1.5 and 9.4 T using MRI relaxometry. The obtained values provide the crucial quantitative link between MRI parameters and neuronal iron distribution, which is an important step toward *in vivo* characterization of DNs in health and disease.

II. THEORETICAL CONSIDERATIONS

DNs in the substantia nigra pars compacta contain paramagnetic iron accumulated in the pigment neuromelanin in the soma [11] [Figs. 1(c) and 2(a)]. In a static magnetic field, iron within these cells builds up magnetization. The resulting magnetic moment of the DNs is proportional to the product of the mass of iron in the DN, the magnetic susceptibility of that iron, and the magnetic field [Fig. 1(a)]. In the following, we demonstrate that the magnetic moment of a DN can be quantified using MRI microscopy. The magnetic susceptibility of neuromelanin-bound iron is then determined by comparing the magnetic moment of each neuron to the mass of the iron the neuron contains.

The magnetic moment of a DN perturbs the magnetic field nearby and alters the Larmor frequency of protons, making it spatially dependent $\omega(r)$ [Figs. 1(a) and 2(d)]. These frequency perturbations manifest themselves in two ways in gradient-echo (GE) MRI images: first, as phase shifts of GE images [Fig. 2(d)]; second, as the effective transverse relaxation rate R_2^* induced by the dephasing of the GE signal [36] [Fig. 2(e)].

In Secs. II A and II B, we develop a biophysical model describing GE signals of tissue containing DNs for ultra-high-resolution MRI microscopy, approximating neurons as magnetized spheres.

In conventional MRI, the size of the structure of interest (for instance, brain nuclei) is usually much larger than the voxel size, which is itself much larger than the typical diffusion length of water on the timescale of the MRI acquisition (approximately equal to several μm for the typically used echo times of tens of ms). In contrast, the size of the structures of interest in MRI microscopy (i.e., neurons with sizes of about 10 to 20 μm) is similar to the voxel size (approximately 20 μm) as well as to the

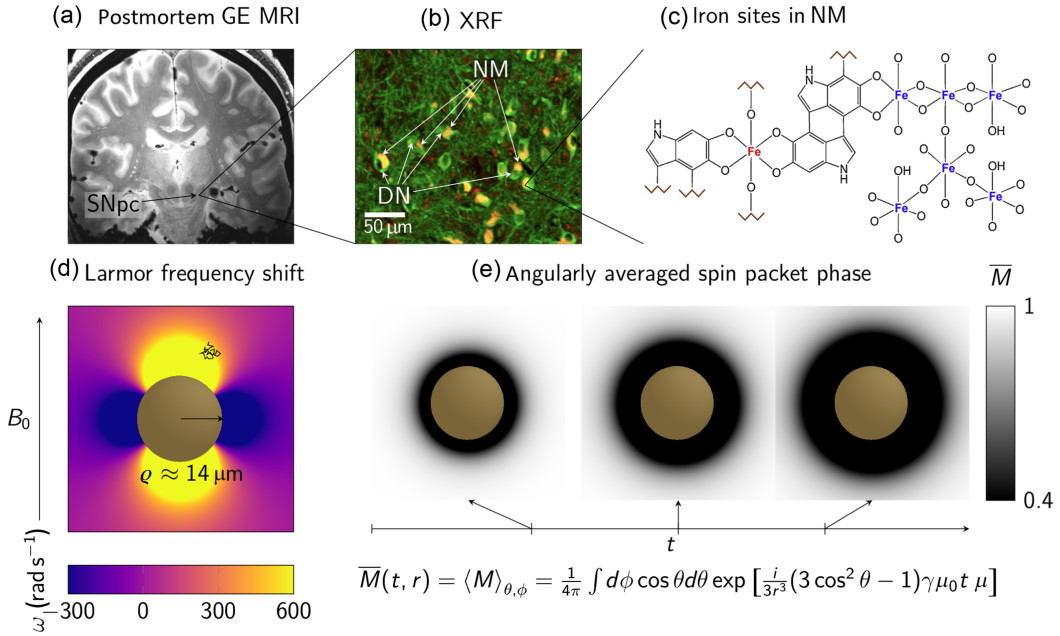

FIG. 2. Biophysical model of the MRI microscopy of a neuromelanin cluster in the soma of a dopaminergic neuron in the SNpc. (a) An iron-sensitive GE MRI image shows the SNpc as an oval region of hypointense signal in the brainstem. MRI data were taken from an openly accessible multimodal postmortem histology and MRI dataset [37]. (b) DNs (green) contain clusters of iron-rich pigment NM (yellow). DNs were stained with nickel-enhanced anti-tyrosine-hydroxylase immunohistochemistry. We show an overlay of nickel (green) and iron (red) concentration maps acquired with XRF imaging, in which iron-rich NM within the nickel-marked DN somata appear yellow. (c) Neuromelanin has two iron-binding sites with distinct magnetic properties and an unknown share of the total iron load: a mononuclear (red) and a crystalline binding site (blue). Figure reproduced from Ref. [11] with permission. (d) Disregarding smaller length scales, we modeled the mesoscopic effect of iron-rich neuromelanin clusters on the MRI signal by approximating them as homogeneously magnetized spheres with a radius $\varrho = 14$ μm estimated from histology. The resulting cross-shaped magnetic dipole field around the NM cluster perturbs the Larmor frequency sensed by water protons diffusing in their vicinity (indicated with a black line). (e) In a GE experiment, the perturbed Larmor frequency of water protons around the NM cluster leads to loss of phase coherence, creating a dephased volume. The radius of this approximately spherical volume grows as $r \sim t^{1/3}$, leading to the typical linear-exponential signal decay in the static dephasing regime. That behavior is illustrated by the angularly averaged spin package phase Eq. (14) as an estimate of dephasing within an imaging voxel.

diffusion length of water protons. Therefore, our description of the GE signal accounts for the effect of diffusion (Sec. II C) and for the finite size of the point-spread function of MRI imaging (Sec. II D). The effect of the shape of DNs is described in the Appendix.

Our model quantitatively links the magnitude and phase of GE images in the presence of a DN to magnetic moments of that DN. We determined the susceptibility of iron in neuromelanin by comparing these magnetic moments with DN iron mass determined with PIXE and XRF [Fig. 1(b)].

Eventually, that susceptibility value was used to describe the collective effect of DN on conventional MRI relaxometry obtained at macroscopic resolutions using static dephasing theory as described in Sec. II E [Fig. 1(b)].

A. Gradient-echo MRI microscopy of magnetic inclusions in the tissue

In this subsection, we describe the gradient-echo MRI signal formation for an imaging experiment at microscopic resolution.

Consider the tissue containing iron-rich cells exposed to the static magnetic field B_0 of an MRI scanner. The Larmor frequency ω varies spatially due to magnetic-field perturbations induced by the cellular distribution of paramagnetic iron. Assume the diffusion coefficient is $D(\mathbf{r})$ and the transverse relaxation rate $R_2(\mathbf{r})$ are local tissue parameters. The latter results from fast molecular processes and short-range molecular interactions, well averaged on the time-scale of MRI experiments (correlation times $\ll 1$ ms) [38].

In a GE experiment, the excitation radio-frequency pulse creates transverse magnetization denoted here as a complex-valued quantity $M = M_x + iM_y$. Its evolution is described by the Bloch-Torrey equation [39]

$$\frac{\partial}{\partial t}M = \left[\frac{\partial}{\partial \mathbf{r}}D(\mathbf{r})\frac{\partial}{\partial \mathbf{r}} - R_2(\mathbf{r}) - i\Omega(t,\mathbf{r})\right]M, \qquad (1)$$

where $\Omega(t,\mathbf{r})$ is the offset in the Larmor frequency due to the presence of magnetized cells and applied imaging magnetic-field gradients that alter the Larmor frequency by $\mathbf{g}(t)\mathbf{r}$. Since the magnetic-field perturbations induced by metal within the cells $\omega(\mathbf{r})$ is constant in time, $\Omega(t,\mathbf{r}) = \omega(\mathbf{r}) + \mathbf{g}(t)\mathbf{r}$.

The measured decay of the transverse magnetization is the integral over the magnetization M of all spin packets

$$S(t) = \int \frac{d^3\mathbf{r}_0}{V} M(t,\mathbf{r}_0), \qquad (2)$$

where M is the solution of Eq. (1) and V the sample volume.

MR imaging is enabled by applying the imaging field gradient $\mathbf{g}(t)$ in Eq. (1). Our highest MRI microscopy resolution of $(22\ \mu\text{m})^3$ is much larger than the diffusion length during the maximum echo time in a given direction estimated as $\sqrt{2DT_E} \approx 4$ μm for an experimentally determined diffusion coefficient in postmortem formalin-fixed tissue $D = 0.3\ \mu\text{m}^2/\text{ms}$ [10] and the maximum echo time $T_E = 25$ ms. In this case, $\mathbf{g}(t)$ is so weak that we approximate the resulted frequency offset $\mathbf{g}(t)\mathbf{r} \approx \mathbf{g}(t)\mathbf{r}_0$ as constant over the diffusion length of spin-bearing protons (For the case of *in vivo* MRI, for instance, on unfixed human tissue or lab animals, the approximation of a constant imaging gradient is valid for most cases. *In vivo*, an increased diffusion coefficient of $D = 1\ \mu\text{m}^2/\text{ms}$ leads to an increased diffusion length of approximately 7 μm during the same echo time as above, which slightly increases the minimum voxel size for which that approximation is appropriate. Nevertheless, as typical voxel sizes in *in vivo* MRI are much larger than 22 μm, the approximation holds.). Such a constant term results in the factorizable exponential factor in the solution of Eq. (1)

$$\begin{aligned} M(t,\mathbf{r}_0) &= M_1(t,\mathbf{r}_0)\exp\left[-i\int_0^t dt'\mathbf{g}(t')\mathbf{r}_0\right] \\ &\equiv M_1(t,\mathbf{r}_0)e^{-i\mathbf{k}(t)\mathbf{r}_0}. \end{aligned} \qquad (3)$$

This renders the signal the Fourier transform of $M_1(t,\mathbf{r}_0)$ when substituted in Eq. (2) as in conventional MRI imaging.

B. DNs in SNpc: Model assumptions and approximation by magnetized spheres

Next, we apply the formalism introduced in the previous subsection to the case of MRI signal decay in the SNpc. The SNpc has a low density of myelinated fibers and contains mainly neuromelanin-pigmented iron-rich dopaminergic neurons [Fig. 2(b)] and glia cells [2]. To create a biophysical model of MRI microscopy of DN in SNpc, we make several simplifying assumptions.

(i) Iron is the main source of Larmor frequency perturbations $\omega(\mathbf{r})$. Iron is a strong contributor to spin dephasing in brain tissue [40], and the predominant magnetic perturber in the SNpc, which contains only few myelinated fibers [10,19]. Chemical iron removal removes the GE contrast within SNpc, justifying the above assumption [10].

(ii) Only iron in dopaminergic neurons contributes meaningfully to the spatial variation of $\omega(\mathbf{r})$. By making this assumption, we neglect all other potential contributions, including the ferritin-bound iron in brain cells other than dopaminergic neurons such as glia cells [2,10]. Indeed, histological stains showed that ferritin-bound iron is distributed relatively homogeneously and varies on a larger length scale of approximately 100 μm [10], much larger than typical cell sizes. Hence, we can assume that ferritin-bound iron contributes to a spatially homogeneous R_2 and also introduce a homogeneous

background phase ϕ_{BG} and Larmor frequency shift ω_{BG}, leading to a factorizable exponent

$$M_1(t,\mathbf{r}_0) = \psi(t,\mathbf{r}_0)e^{-R_2 t - i(\phi_{\mathrm{BG}}+\omega_{\mathrm{BG}}t)}. \quad (4)$$

Strictly speaking, factoring $e^{-R_2 t}$ holds without further assumptions only outside of DNs, as we assume that there is no ferritin-bound iron in DNs. Nevertheless, we use the factorization for the whole volume without further restrictions because we exclude the inside of the DN from the magnetic moment quantification to desensitize the method to DN shape (see Sec. IV C).

(iii) The diffusion coefficient D is spatially homogeneous. Since the SNpc contains few myelinated fibers, it is plausible to assume that there is no preferred diffusion direction, and D is therefore isotropic. Assuming a spatially homogeneous D, we show that the effect of diffusion on the GE signal decay is negligible (Sec. II C). This justifies in a self-consistent way the simplification of neglecting effects of inhomogeneous diffusion, e.g., due to DN membranes.

(iv) The field perturbation induced by DNs is well described by the magnetic field of a dipole. The validity of this approximation is justified in Sec. VIII, where we show that higher multipole moments are negligible for compact paramagnetic objects such as cell bodies and further supported by numerical simulations for other canonical shapes such as cones.

To generate the dipole field, we model the DN soma as a sphere with a radius ϱ and constant volume susceptibility, which differs from the susceptibility of the surrounding tissue by χ_{v} [Fig. 2(d)].

This volume susceptibility is linked to the iron content of the DN soma. As before [10], in the following, we assume that all iron within the DN soma is bound by neuromelanin. Thus, χ_{v} is the difference between the volume susceptibility of a DN soma determined by its iron concentration c, and the volume susceptibility of the surrounding tissue determined by the concentration of ferritin-bound iron c_{FT} in the vicinity of the DN soma:

$$\chi_{\mathrm{v}} = \chi_\rho c - \chi_{\rho,\mathrm{FT}} c_{\mathrm{FT}}, \quad (5)$$

where χ_ρ is the unknown mass susceptibility of iron in neuromelanin, and $\chi_{\rho,\mathrm{FT}} = 1.24\times10^{-6}$ m^3/kg the mass susceptibility of iron in ferritin [41]. In this case, the mass of iron in a DN soma is given by $m = (4\pi/3)c\varrho^3$. However, it is not clear whether all iron in DN somata is bound by other forms such as ferritin. Elemental mapping methods (XRF and PIXE) are not sensitive to the chemical form of iron binding, and therefore this question cannot be addressed experimentally. To account for this ambiguity, as an opposite limiting case, we determine the mass susceptibility of neuromelanin assuming that the concentration of ferritin-bound iron is homogeneous throughout the tissue, including DN somata. In this case, the volume susceptibility is $\chi_V = (c - c_F T)\chi_\rho$, while the mass of iron in neuromelanin is given by $m = (4\pi/3)(c - c_{\mathrm{FT}})\varrho^3$.

In a static magnetic field B_0, the magnetization of the DN soma builds up, resulting in a magnetic moment along the z axis:

$$\mu = \frac{B_0}{\mu_0}\frac{4\pi}{3}\varrho^3\chi_{\mathrm{v}}, \quad (6)$$

where μ_0 is the vacuum permeability. Note that this equation links the MRI-detectable magnetic moment of a DN with its iron mass, which we assessed independently.

The dipole field outside the sphere leads to a Larmor frequency shift of water protons

$$\omega(\mathbf{r}) = \delta\omega\frac{\varrho^3}{r^3}(3\cos^2\theta - 1) = -\frac{\gamma\mu_0\mu}{4\pi r^3}(3\cos^2\theta - 1), \quad (7)$$

where $\delta\omega = (\omega_0/3)\chi_{\mathrm{v}}$ is the characteristic shift of the Larmor frequency $\omega_0 = \gamma B_0$ at the DN soma's equator, r is the distance of the proton to the DN soma (regular font stands for the length of corresponding vectors), and θ the angle between B_0 and $\mathbf{r}$ [Fig. 2(d)].

In practice, the DN magnetic moment can be quantified only if it is high enough to have a measurable impact on the GE signal. Thus, we restrict the analysis here to a minimum DN magnetic moment of $\mu = 64$ mA μm^2, which turns out to be the lower bound of reliable magnetic moment quantification from the acquired data. At constant ϱ and $B_0 = 9.4$ T, that defines a lower bound of DN volume susceptibility of $\chi_{\mathrm{v}} = 10^{-6}$ and a characteristic Larmor frequency shift of $\delta\omega \approx 0.84$ ms^{-1}.

The dipole field Eq. (7) around a DN soma produces a growing volume in which water protons are dephased and contribute only little to the MRI signal [38]. We can approximate this dephased volume as a sphere with effective radius r_d chosen so that the protons at the sphere surface accumulate a phase difference ϕ of the order of unity [Fig. 2(e)] at time t after the excitation pulse

$$\phi \approx \frac{\delta\omega\times\varrho^3}{r_d^3}\times t = 1 \Leftrightarrow r_d \approx \sqrt[3]{\delta\omega t}\varrho. \quad (8)$$

The dephased sphere at the highest experimental echo time of 25 ms for the minimum DN magnetic moment of 64 mA μm^2 we consider is $r_d \approx 38$ μm. Equation (7) indicates that the Larmor frequency changes appreciably over the distance to the DN soma, r_d. As estimated above, the diffusion length at this echo time is 4 μm, hence, so low that it encompasses only a small perturbation of the Larmor frequency. Therefore, we can approximate the field within a spin package observed during the measurement time with the first two terms of its Taylor expansion,

$$\omega(\mathbf{r}) \approx \omega(\mathbf{r}_0) + (\mathbf{r}-\mathbf{r}_0)\cdot\frac{\partial}{\partial\mathbf{r}}\omega(\mathbf{r})\Big|_{\mathbf{r}=\mathbf{r}_0}. \quad (9)$$

The propagator of the Bloch-Torrey Eq. (1) is known for a linear field with a constant gradient $\mathbf{g} = (\partial/\partial\mathbf{r})\omega(\mathbf{r})|_{\mathbf{r}=\mathbf{r}_0}$,

$$\mathcal{G}(t,\mathbf{r}_1,\mathbf{r}_0)=\frac{1}{(4\pi Dt)^{3/2}}\exp\left[-\frac{(\mathbf{r}_1-\mathbf{r}_0)^2}{4Dt}-\frac{i}{2}\mathbf{g}\cdot(\mathbf{r}_1-\mathbf{r}_0)t-\frac{1}{12}Dg^2t^3\right]e^{-i\mathbf{g}\mathbf{r}_0t}. \quad (10)$$

Integrating this propagator over the sample volume, assuming an initially homogeneous magnetization, we obtain [42]

$$\psi(t,\mathbf{r}_0)=\exp\left(\underbrace{-\frac{1}{3}Dg(\mathbf{r}_0)^2t^3}_{\text{diffusion}}\underbrace{-i\omega(\mathbf{r}_0)t}_{\text{phase}}\right). \quad (11)$$

The first term in the exponent describes the signal decay due to water diffusion along $g=|\mathbf{g}|$, while the second term describes the phase of spin isochromates.

C. Impact of diffusion

Next, we show that the diffusion term in Eq. (11) is negligible for DNs with magnetic moments larger than the minimum magnetic moment of $\mu = 64$ mA μm^2 introduced above. Diffusion averages most effectively over the Larmor frequency perturbation closest to the DN soma. Hence, we estimate the diffusion term at the boundary of the dephased sphere defined in Eq. (8) as an upper bound of diffusion effects.

An order-of-magnitude estimate of the frequency gradient g near a dopaminergic neuron soma can be obtained by differentiating the order-of-magnitude estimate of Eq. (7):

$$g\approx\frac{\delta\omega\varrho^3}{r^4}. \quad (12)$$

That allows us to estimate the diffusion factor in Eq. (11):

$$\exp\left(-\frac{1}{3}Dg^2t^3\right)=\exp\left(-\frac{1}{3}\times\frac{(\delta\omega t)^{1/3}}{\delta\omega\tau_D}\right)\approx\exp(-1.6\times10^{-3})\approx1, \quad (13)$$

where the diffusion time across the neurons is $\tau_D=\varrho^2/D\approx650$ ms, $t=25$ ms, and $\delta\omega=0.84$ ms^{-1} as above. Hence, water diffusion affects the GE decay negligibly, and relaxation is described well by the static dephasing regime [36]. [For the case of *in vivo* MRI, the static dephasing regime still applies, as the threefold-higher diffusion coefficient would not alter the validity of the approximation in Eq. (13).]

In this case [36], Eq. (11) in the DN-centered coordinate system of Eq. (7) simplifies to [42]

$$\psi(t,r,\theta)=\exp\left(\frac{i}{3r^3}(3\cos^2\theta-1)\gamma\mu_0t\mu\right). \quad (14)$$

D. Impact of the point-spread function of MRI microscopy

We now take into account additional averaging due to the limited resolution of the imaging experiment. In a GE image with cellular resolution, the complex-valued MRI signal around a DN soma described by Eq. (2) can be measured only with limited spacial resolution, leading to the partial spatial averaging over the voxel described by Eq. (3). As we record the signal in the Fourier domain, the point-spread function in imaging space is a three-dimensional sinc function. Thus, the signal we record from an imaging voxel is described by

$$S(t,\mathbf{r}_0)=e^{-R_2t-i(\phi_{\mathrm{BG}}+\omega_{\mathrm{BG}}t)}\int\frac{d^3\mathbf{r}}{8\pi^3V}\exp\left(\frac{i}{3r^3}(3\cos\theta-1)\gamma\mu_0t\mu\right)\mathrm{sinc}\left(\frac{x-x_0}{2L}\right)\mathrm{sinc}\left(\frac{y-y_0}{2L}\right)\mathrm{sinc}\left(\frac{z-z_0}{2L}\right), \quad (15)$$

where $\mathbf{r}_0=(x_0,y_0,z_0)$ is the voxel location and L the voxel size [43].

Our goal is to quantify the magnetic moment μ of the cell by fitting Eq. (15) to the GE signal of voxels around an individual neuron. DNs in SNpc are rather sparse, which allows for studying isolated DNs. To this end, we need an MRI protocol that achieves sufficiently small L to image the impact of isolated DNs ($\rho\sim14$ μm) on the GE signal. MRI microscopy on postmortem brain tissue at ultrahigh-B_0 field (≥9.4 T) achieves voxel sizes as low as approximately 20 μm [indicated in Fig. 2(b)]. Moreover, we employed a superresolution approach by fitting the mesoscopic model MRI signal [Eq. (14)] convolved with the point-spread function to the MRI signal [Eq. (15)]. We found a balance between considering voxels that are close to the DN and hence are affected strongest, but not directly next to the soma to ensure that the far-field approximation of the dipole field holds (see Sec. IV C). For computational efficacy, we calculated the integral in Eq. (15) in the Fourier domain [44]. To estimate the mass susceptibility of iron in neuromelanin, we used Eq. (6) and combined the magnetic moment quantification with iron quantification in the same DN using PIXE and XRF.

E. MRI relaxometry

The determined mass susceptibility of neuromelanin-bound iron can be used to link the cellular iron loads of DNs and their density to maps of quantitative susceptibility and effective transverse relaxation rate acquired with

conventional macroscopic resolutions. In cases when MRI voxels extend over several 100 μm, encompassing many DNs, Eq. (15) does not apply as it accounts only for one DN. Static dephasing theory [36] describes the collective impact of multiple DNs on the GE signal in case of negligible water diffusion. The theory predicts a regime of linear decay for times larger than $3/(2\delta\omega) \approx 1.8$ ms, encompassing all relaxometry echo times we used. In this regime, the effective transverse relaxation rate induced by DNs is given by [36]

$$R_2^* = \frac{2\pi}{9\sqrt{3}}\omega_0\chi_\rho\zeta c, \tag{16}$$

where ζ is the volume fraction of DNs.

We assessed the validity of the static dephasing regime modeling at three clinically used magnetic-field strengths (1.5, 3, and 7 T) for *in vivo* and postmortem tissue using a Monte Carlo simulation informed by histological 3D iron concentration maps in the substantia nigra pars compacta (see Sec. III I), following a previously published approach [10].

III. METHODS

First, we quantified the magnetic moment of dopaminergic neurons using MRI microscopy at 9.4 T and numerical simulations. Second, we determined the iron load of DNs using PIXE, micro-x-ray fluorescence, and immunohistochemistry. Subsequently, we obtained the susceptibility of iron bound to neuromelanin at 9.4 T *in situ* using a linear regression of the magnetic moments versus iron load of different DNs. Third, we extrapolated our results to clinical magnetic-field strengths using relaxometry at varying B_0.

A. Postmortem human brain tissue samples

Two midbrain samples including left substantia nigra from human postmortem brains were provided by the Brain Banking Center Leipzig of the German Brain Net (GZ 01GI9999-01GI0299) operated by the Paul Flechsig Institute of Brain Research (Approval No. 82-02). Brain material was obtained at autopsy with prior informed consent and approved by the responsible authorities. Sample 1 with size $3 \times 3 \times 15$ mm^3 was donated by an 86-year-old male, who died of heart failure. Sample 2 with the size of $5 \times 15 \times 11$ mm^3 was donated by a 61-year-old male, who died from renal failure. The postmortem interval before fixation was less than 24 h for all tissue samples. Following the standard brain bank procedures, blocks were immersion fixed in 4% paraformaldehyde in phosphate-buffered saline (PBS) at *p*H 7.4 for at least six weeks to ensure complete fixation. Before the MRI experiments, tissue blocks were washed in PBS with 0.1% sodium azide to remove formaldehyde residues from the tissue.

B. MRI microscopy

For MRI microscopy, fixed tissue samples were placed in plastic syringes of 22 mm diameter and immersed in proton-free fluid Fomblin (Solvay Solexis, Bollate, Italy) to eliminate MRI signal from outside the sample. MEGE images with an ultrahigh isotropic resolution of 22 μm (sample 1) and 24 μm (sample 2) were acquired at 9.4 T using a helium-cooled two-channel quadrature mouse coil [Figs. 3(a) and 3(b)]. Table I gives an overview of all MRI sequence parameters. All magnitude and phase images were reconstructed from the raw data using in-house developed MATLAB routines and stored. For ultrahigh-resolution MEGE images, complex-valued data from the two channels were averaged after the removal of phase offsets between repetitions and individual channels using the MCPC 3D S method [45]. Single-echo gradient-echo images with a high isotropic resolution of 60 μm were acquired at 7 T and used for registration to 9.4 T MEGE data.

C. Relaxometry

MRI relaxometry was performed at static magnetic-field strengths B_0 of 1.5, 3, 7, and 9.4 T. MEGE images with an isotropic resolution of 220 μm were acquired at 7 and 3 T as part of a multiparameter mapping acquisition (all parameters in Table I) [46]. All magnitude and phase images were reconstructed and stored as above. Furthermore, single-channel MEGE data acquired at 9.4 T were downsampled to the resolution of the MEGE data at lower fields and processed in the same manner for the assessment of the B_0 scaling behavior of R_2^*. Quantitative parameter maps of R_2^* were calculated from the high-resolution MEGE magnitude images using a exponential fit with a Rician noise floor implemented in the PYTHON programming language.

D. Superresolution magnetic moment estimate

We estimated the magnetic moment of the preselected DNs, which fulfilled two conditions: (i) They were reliably identified on histological images and completely included in the quantitative iron maps; (ii) on histological images, they were well separated from other DNs, so their individual magnetic moment could be robustly fitted.

The magnetic moment of these DNs was determined by fitting the predicted complex-valued signal of the biophysical model [Eq. (15)] to the ultrahigh-resolution MEGE images (Fig. 4).

The DN soma was modeled as a sphere with radius $\varrho = 14$ μm, which was the average radius of randomly selected large neuromelanin clusters on microscopy images.

The Larmor frequency shift around the DN soma was simulated at an isotropic resolution of 1 μm using Eq. (7) [Fig. 4(a)].

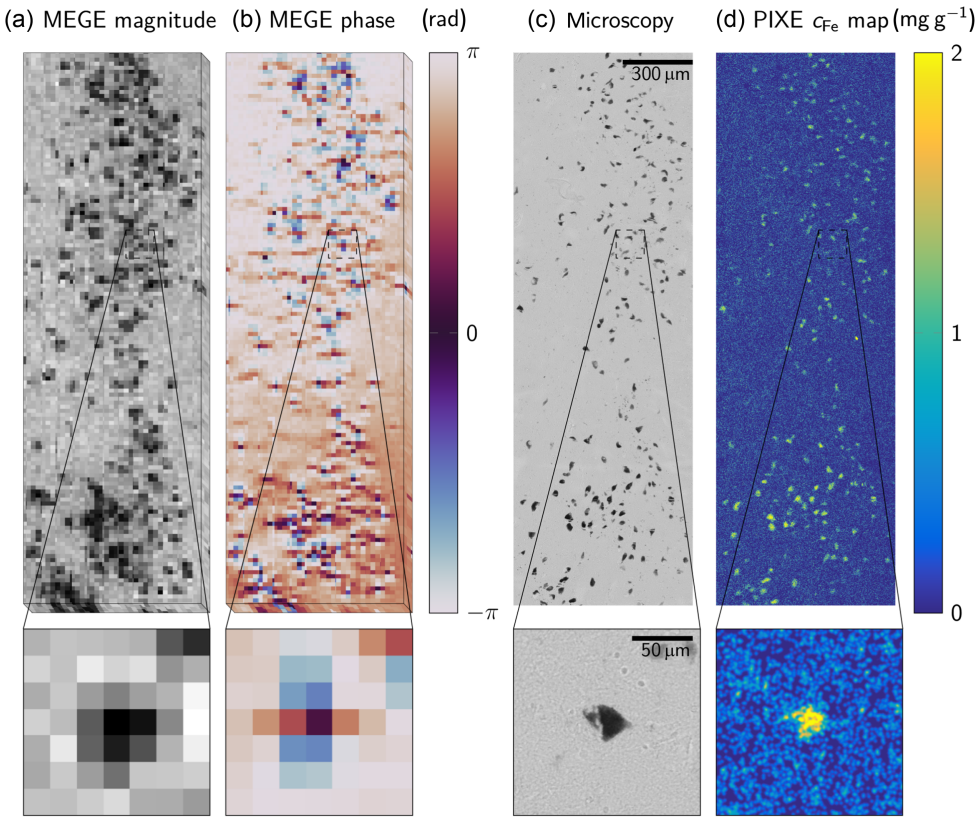

FIG. 3. Combining superresolution MRI and ion-beam microscopy for *in situ* magnetometry of iron in human DNs. The top row shows an overview image, while the insets on the bottom row show the signature of a single DN soma in different imaging modalities. (a) The magnitude of T_2^*-weighted MEGE images shows DN cell bodies (somata) as areas with hypointense signal over several imaging voxels. The magnitude image resembles a low-resolution sampling of Fig. 2(e). The growth of the dephased sphere in multiecho data is shown in Fig. 4. (b) The phase of MEGE images around DN somata is perturbed in the cross shape expected for dipole fields. The phase is similar to a low-resolution sampling of Fig. 2(d). The complex-valued MEGE data were used to quantify the magnetic moment of individual DN somata (Fig. 4). (c) In unstained light microscopy images of histological sections, clusters of the pigment neuromelanin within DN somata are visible. (d) Quantitative iron maps acquired with ion-beam microscopy using PIXE show an elevated iron concentration at the location of neuromelanin clusters seen in (c) (inset). The iron content of an individual DN was quantified on consecutive sections to account for partial volume effects (see Fig. 5).

TABLE I. Overview of MRI sequence parameters of GE and MEGE sequences at different static magnetic-field strengths B_0.

Field strength (T)	1.5	3	7	9.4
Scanner	Avanto, Siemens Healthineeers, Erlangen	Connectom, Siemens Healthineeers, Erlangen	Magnetom, Siemens Healthineeers, Erlangen	BioSpec 94/20 AV3HD, Bruker, Ettlingen
Receive coil	Four-channel coil	Custom-built two-channel quadrature coil	Custom-built two-channel quadrature coil	Helium-cooled two-channel quadrature coil
MEGE parameters				
Resolution µm^3	208 × 210 × 208	210 × 214 × 214	223 × 220 × 223	22 × 22 × 22
Matrix size	126 × 128 × 192	120 × 150 × 192	224 × 128 × 224	672 × 608 × 320
First echo time (ms)	3.8	3.4	4	5
Echo spacing (ms)	8	2.6	3.3	5.4
Number of echoes	10	16	12	4
Repetition time (ms)	100	60	95	110
Flip angle (deg)	25	80	27	23
Bandwidth (Hz/pixel)	230	490	343	297

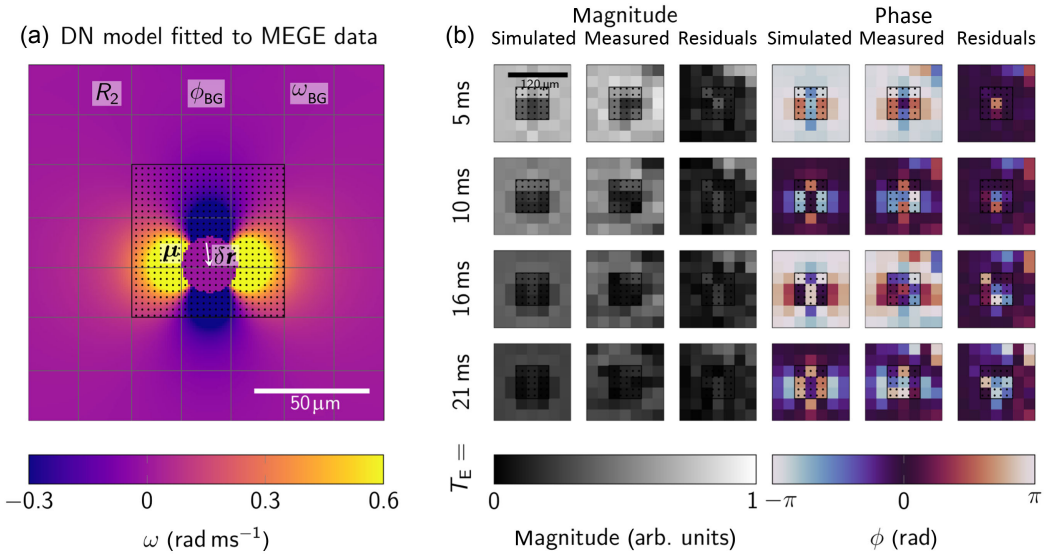

FIG. 4. Magnetic moment of individual DN somata estimated by fitting the dipole approximation of the DN-induced magnetic-field perturbation to complex-valued MEGE MRI microscopy data. (a) The Larmor frequency perturbation of a DN soma that best explains the MEGE MRI data (b). During the fitting of Eq. (14) to MRI data, free parameters were the magnetic moment of the DN soma μ, the position of the center of mass of the DN soma $\delta\boldsymbol{r}$, the complex-valued MR signal at zero echo time $\psi|_{t=0} = \psi_0 e^{i\phi_0}$ defined by its real-valued magnitude ψ_0 and phase ϕ_0, the effective transverse relaxation rate of the tissue around the DN soma $R^*_{2,\mathrm{BG}}$, and the Larmor frequency shift of that tissue ω_{BG}. A black dotted square marks the volume around the DN that we excluded from fitting to desensitize the fit to DN nonsphericity. (b) MEGE MRI microscopy magnitude (left columns) and phase data (right columns) as predicted by our model [(a), first column for magnitude and phase, respectively), measured experimentally (second column), and the fit residuals (third column). The residuals of the magnitude and phase data were calculated as the absolute value of the differences between the simulated and measured magnitude and phase maps, respectively. A dotted square covers the voxels that were disregarded in the fit, corresponding to the black square in (a). The model captures the growth of the dotlike hypointensity in the magnitude images with echo time T_{E} [see Fig. 2(e)]. The model accurately predicts the cross-shaped phase perturbation at the first three T_{E} [see Fig. 2(d)] before the pattern in the experimental data is lost due to low signal-to-noise ratio at the latest T_{E}.

The location of the center-of-mass $\delta\boldsymbol{r}$ was determined at this resolution, an order of magnitude more precise than the size of the MRI voxel size [Fig. 4(a)].

Further free parameters of the model were the complex-valued MR signal at zero echo time $\psi|_{t=0} = \psi_0 e^{i\phi_0}$ defined by its real-valued magnitude ψ_0 and phase ϕ_0, the effective transverse relaxation rate of the tissue around the DN soma $R^*_{2,\mathrm{BG}}$, and the Larmor frequency shift of that tissue ω_{BG}. The background parameters were assumed to be homogeneous within the simulated volume of $7 \times 7 \times 7$ MRI microscopy MEGE voxels around the DN soma.

The parameters best explaining the MEGE data were determined by minimizing the least-squares deviation of the simulated and measured complex-valued signals using the bounded L-BFGS-B algorithm implemented in SciPyv1.6.2 [47].

The parameters were bounded to physically realistic values. A minimum DN magnetic moment of 64 mA µm^2 was required to ensure that the minimization preserved the DN soma.

If boundary values were found as an optimum, the respective DN soma was excluded from further analysis. We excluded the 27 central voxels around each DN from the minimization to exclude the effect of nonsphericity of the DN (Sec. IV C).

The convergence of the minimization was accelerated by first minimizing on a coarser length scale of $(3\ \mu\mathrm{m})^3$ and using the result as an initial guess for the fitting at the finer resolution of $(1\ \mu\mathrm{m})^3$.

The optimum value of $\delta\boldsymbol{r}$ was determined in a separate grid search. The above optimization and the grid search were repeated until the grid search did not find a new optimum position. The error of μ was estimated using bootstrapping, assuming that the fit result was a good approximation of the ground truth. Next, we randomly redistributed the model's residuals 200 times and fitted the model. We used the standard deviation of the resulting distribution of susceptibility values as an estimate for the uncertainty of χ_Q.

E. Histology and immunohistochemistry

Tissue blocks were processed for histochemistry and iron quantification using ion-beam microscopy and XRF as described in detail before [10]. In short, samples were embedded in paraffin and cut into 10-µm sections while recording block-face images for initial alignment to MRI.

Sections were left unstained for tissue iron quantification. Sections were imaged with light microscopy using an ZEISS Axio Scan.Z1 slide scanner (ZEISS, Jena, Germany). For PIXE and XRF, sections were deparaffinized, embedded in mounting medium (DePeX, Merck Millipore, Darmstadt), and subsequently placed in aluminum frames.

F. Cellular iron quantification

Iron concentrations inside DNs were determined using two independent methods: PIXE at the LIPSION proton accelerator (Leipzig University, Leipzig, Germany) and XRF at the Deutsches Elektronen Synchrotron (DESY, Hamburg, Germany). Five unstained, consecutive sections from each sample were deparaffinized, embedded in a foil of mounting medium (DePeX, Merck Millipore, Darmstadt), and subsequently placed into aluminum frames. PIXE was performed using a proton beam of 2.25 MeV and 0.5 nA with a diameter of 0.8 μm. It locally knocked out inner shell electrons, leading to element-specific x-ray emission. The energy dispersive spectra of emitted x rays were recorded by four silicon drift detectors (SDDs, Ketek, Vitus H15, Munich) placed in an optimized geometry with total solid angle coverage of 1.2 sr. Rutherford backscattering spectra were recorded for absolute concentration calculations. On each section, PIXE was performed on regions of interest in the SN with the following parameters: matrix size 1300×3900, field of view 1×3 mm^2, average deposited charge determined by calibrated upstream pickup current integrator [48] 4.2 μC ranging from 2.8 to 6.5 μC between sections. Iron concentration maps were obtained using the GeoPIXE II software (CSIRO, Clayton, Australia) following Ref. [49].

To assess the accuracy of the PIXE tissue iron quantification with an independent second method, XRF iron quantification on one section of sample 1 was performed at the microprobe beamline P06 [50] of PETRA III at DESY (Hamburg, Germany). The high-brilliance x-ray beam was monochromatized at an energy of 12 keV using a cryocooled Si-111 double-crystal monochromator. Kirkpatrick-Baez mirrors in combination with a prefocusing compound refractive lens were used to focus the x-ray beam down to a size of 2×1 μm^2, resulting in a flux of 3×10^{11} photons per second in focus. The incoming flux was measured with an ion chamber placed between the Kirkpatrick-Baez mirrors and the sample while the transmitted flux was measured using a passivated implanted planar silicon diode downstream of the sample. XRF detection was performed using an energy-dispersive four-element SDD (Vortex-ME4, SII Nanotechnology, Northridge, USA) placed with an angle of 225° with respect to the forward direction of the x-ray beam. During the measurement, the sample was continuously scanned through the focus using a nominal step size matching the resolution and a dwell time of 3 ms.

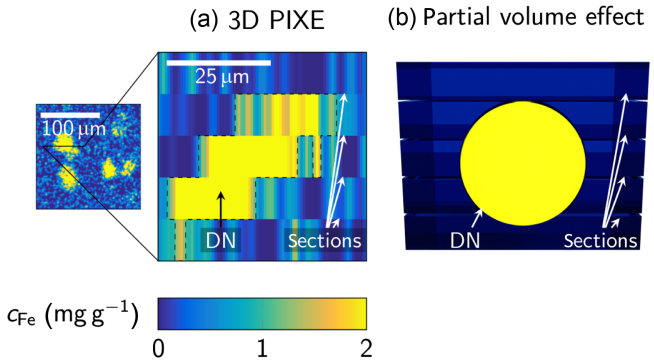

FIG. 5. Iron quantification in DN somata using 3D-reconstructed PIXE. (a) The iron content of individual DN somata (marked with dashed line) was quantified in iron concentration maps obtained on consecutive histological sections, as the average diameter of NM clusters in the DN somata of 14 μm was larger than the histological section thickness of 10 μm. (b) The illustration shows the partial volume effect due to subdivision of a single DN soma on several histological sections.

XRF data evaluation was performed using nonlinear least-squares fitting as implemented in PyMca [51]. For elemental quantification, a thin-film XRF reference sample (type RG-200-0510-C00-X, AXO Dresden GmbH, Dresden, Germany) was measured. The reference sample contained the elements Ti, Cr, Fe, and Cu on a Si substrate. Additional quantification of other elements was calculated from the results of the reference measurement using parameters defined in the software XRAYLIB [52].

We quantified the mass of iron in the identified DNs using 3D reconstructed iron concentration maps (Fig. 5). These maps were obtained by rigidly registering the iron concentration maps to unstained microscopy images using iron-rich, neuromelanin-pigmented clusters as landmarks. We used the alignment between the consecutive microscopy images to reconstruct 3D iron concentration maps. We manually segmented the identified DNs on all slices of the 3D microscopy image and integrated the iron concentration over this volume transformed to the 3D iron concentration map. We assured that the entire DN soma was covered by the PIXE measurement by controlling its absence on the adjacent histological sections.

G. Identifying DN with MRI signal hypointensities

To estimate χ_ρ, we quantified both the magnetic moment and the iron mass for a subset of preselected DNs. To this end, we identified DN somata on histological sections and their corresponding signatures in MRI microscopy images in a two-step procedure.

First, unstained consecutive microscopy sections were stitched into 3D volume using a rigid landmark-based registration. Pigmented DNs, which appeared on several consecutive sections, were used as landmarks.

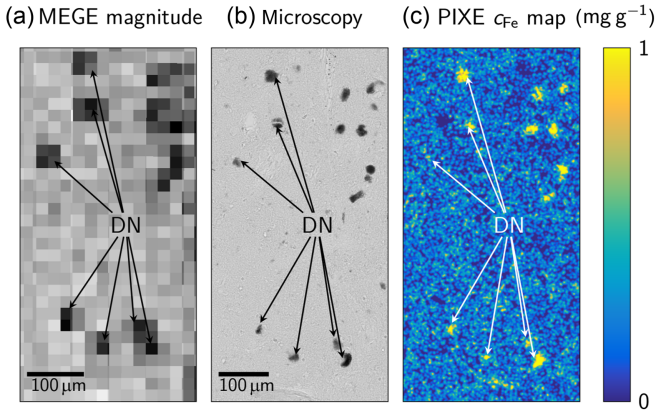

FIG. 6. Registration of ultrahigh-resolution MEGE images (a), light microscopy (b) and iron concentration maps acquired with PIXE (c). For coregistration, matching spatial arrangements of DN somata (marked with arrows) were identified as dotlike magnitude hypointensities in MEGE images (a), dark clusters in microscopy (b), and areas of increased iron concentration (c). 3D microscopy and PIXE images were obtained by registering adjacent microscopy images, using cut DN shared between the sections as landmarks for a rigid registration (not shown). The scale bar shown in (b) and (c) is the same and depicted in (b).

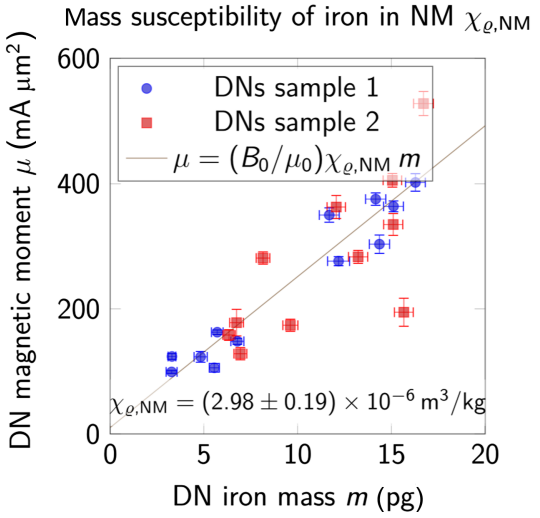

FIG. 7. Determining the mass susceptibility of iron bound to neuromelanin in dopaminergic neurons χ_ρ. Each dot in the scatter plot represents one DN soma with its magnetic moment on the vertical axis and its iron mass on the horizontal axis. Fitting the experimental data with a proportional function (solid line) using an orthogonal distance regression [53], we estimated $\chi_\rho = (2.98 \pm 0.19) \times 10^{-6}$ m^3/kg.

Second, these 3D optical microscopy volumes were registered to MRI microscopy volumes by matching patterns of pigmented DNs with similar patterns of signal hypointensities in the MR images (Fig. 6). An affine transformation was calculated using the DNs in these patterns as landmarks and applied to the MEGE data [Figs. 3(a) and 3(b)].

From the identified DNs, we selected those whose signatures in the MRI microscopy images were well separated from neighboring DNs, so our biophyiscal model of an isolated DN's impact on the MRI microscopy signal is applicable.

H. Quantifying neuromelanin's susceptibility

Based on the iron mass and magnetic moment of the subset of preselected dopaminergic neuron somata, we quantified the mass susceptibility of iron in neuromelanin χ_ρ (Fig. 7). We fitted a linear function to these data using the orthogonal distance regression [53] implemented in the SciPy library, taking into account both measurements' uncertainties.

We repeated the quantification of χ_ρ for the assumption of a homogeneous distribution of iron in ferritin also within the neuromelanin domains of the dopaminergic neurons.

I. Predicting susceptibility and R_2^* at clinical B_0-field strengths

Next, we extrapolated the susceptibility of iron in DN to clinical field strengths. As MRI microscopy is not available at clinical B_0 due to signal-to-noise ratio constraints, we took an indirect approach. We estimated the field dependence of R_2^* using R_2^* maps measured for B_0-field strength from 1.5 to 9.4 T and assumed linear proportionality between R_2^* and susceptibility.

We coregistered the R_2^* maps using a rigid registration in the ANTs software [54].

Static dephasing theory predicts a proportionality of the R_2^* rate induced by DN somata to the DN's magnetic moment, i.e., $R_2^* \propto \mu \propto \chi_\rho B_0$ [36].

We assume that the DNs contribute the major part of the iron-induced effective transverse relaxation rate $R_{2,\mathrm{iron}}^*$ in the DN-rich substantia nigra pars compacta. Note that a smaller part of the $R_{2,\mathrm{iron}}^*$ rate in this region is contributed by ferritin-bound iron, mostly found outside of DNs. Past research showed that the susceptibility of ferritin-bound iron is independent of magnetic field in the range we used here [55]. Thus, if relaxation due to ferritin-bound iron occurs in the static dephasing regime, the contribution of ferritin-bound iron to $R_{2,\mathrm{iron}}^*$ scales linearly with B_0.

Furthermore, we assumed that $R_{2,\mathrm{iron}}^*$ was approximately equal to the B_0-dependent portion of R_2^*: $R_{2,\mathrm{iron}}^*(B_0) = R_2^*(B_0) - R_{2,\mathrm{BG}}^*$, subtracting from the measured R_2^* a field independent, non-iron-induced background rate $R_{2,\mathrm{BG}}^*$.

We quantified the B_0 dependency of $R_{2,\mathrm{iron}}^*$ in the DN-rich substantia nigra pars compacta by fitting the model function

$$\frac{R_{2,\mathrm{iron}}^*(B_0)}{R_{2,\mathrm{iron}}^*(B_0 = 9.4\ \mathrm{T})} = AB_0. \tag{17}$$

Therein, we normalized $R_{2,\mathrm{iron}}^*$ by its value at 9.4 T to simultaneously fit the model to the data of both specimens,

which provided the parameters A and $R^*_{2,\mathrm{BG}}$ assumed to be the same across specimens.

Extrapolating our estimate of χ_ρ to clinical field strengths enabled us to predict the impact of DN somata on the susceptibility and R^*_2 at 3 and 7 T. We obtained DN somata masks by segmenting neuromelanin clusters on unstained histological sections using the Trainable WEKA S Segmentation [56] in the FIJI software [57]. We used the proportionality between optical density in these images and iron concentration in neuromelanin to estimate maps of iron concentration in DNs [10]. From these, we calculated susceptibility maps using Eq. (5). Maps of the R^*_2 rate were estimated using the long-time limit of static dephasing theory [Eq. (16)] [36]. We assumed that the susceptibility difference between the DN somata and the surrounding tissue was approximately equal to the susceptibility induced by iron in the DN somata, as both iron concentration and mass susceptibility of ferritin-bound iron were considerably lower than in DN somata. We obtained estimates of susceptibility and R^*_2 at the resolution of the relaxometry measurements at 3 and 7 T by averaging the quantities in pixels of 220-μm-edge length.

Both extrapolations of our results used the static dephasing approximation, i.e., negligible water diffusion during gradient-echo signal decay [36]. We numerically assessed the validity of the static dephasing approximation in a representative voxel in nigrosome 1 by conducting the Monte Carlo simulation of the GE signal decay in a previously published 3D tissue model based on quantitative iron histology, using a previously developed approach [10]. This approach was updated with the susceptibility of neuromelanin-bound iron obtained in this study. We simulated the GE signal decay using diffusion coefficients typical for *in vivo* and postmortem brain tissue (1 and 0.3 $\mu\mathrm{m}^2/\mathrm{ms}$, respectively) and clinical and ultrahigh-magnetic-field strengths ($B_0 = 1.5$, 3, 7, 9.4 T). We estimated the R^*_2 rates for the simulated decays by fitting an exponential decay function to the predicted GE signals at experimentally plausible echo times as described before [10].

IV. RESULTS

A. Multimodal identification of DN somata

In the MEGE magnitude data of substantia nigra pars compacta, areas of signal hypointensity spanning several imaging voxels were observed [Fig. 3(a)]. In the MEGE phase, cross-shaped perturbations were observed at the location of the dotlike signal hypointensities [Fig. 3(b)]. These signal magnitude and phase perturbations resembled the signal perturbation of magnetic dipoles, empirically supporting our approximation of DN somata as dipoles [Eq. (6); Figs. 2(d) and 2(e)]. On light microscopy images of unstained histological sections, DN somata were visible due to the dark pigment neuromelanin they contained [Fig. 3(c)]. Quantitative iron concentration maps acquired with PIXE and XRF showed an increased iron concentration within the DN somata [Fig. 3(d)].

The spatial arrangement of these DN somata in the light microscopy and PIXE data resembled the spatial arrangement of dotlike and crosslike perturbations in the MEGE magnitude and phase data, respectively. This indicates that the MEGE signal perturbations were due to iron-rich DN somata and that they reliably mapped DN somata. Based on this hypothesis, we identified spatial patterns of dotlike signal hypointensities in MEGE magnitude images with DN somata in 3D-stitched unstained histological sections [Figs. 2(b) and 6], which resulted in a one-to-one assignment of 14 DN somata for each sample.

B. Susceptibility of iron in DN

Next, we estimated the mass susceptibility of iron in neuromelanin χ_ρ in DN somata, comparing the mass of iron m and the magnetic moment μ for a subset of preselected DNs. In the PIXE data, m ranged from (3.8 ± 0.3) to (19.4 ± 0.6) pg (Fig. 5). The accuracy of the m estimates was corroborated by a high correspondence between DN iron quantification using two independent measurements PIXE and XRF (Fig. 10 in Appendix D). Using super-resolution, complex-valued fits of the DN soma model to the MRI data, we found that μ ranged from (90 ± 20) to (550 ± 110) $\mathrm{mA}\,\mu\mathrm{m}^2$ in the same set of DNs (Fig. 4). We excluded DNs whose magnetic moments reached the boundaries of the fit. Data from the remaining 23 DNs (12 DNs in sample 1, 11 DNs in sample 2) allowed us to estimate $\chi_\rho = (2.98 \pm 0.19) \times 10^{-6}$ m^3/kg (mean ±SD), using an orthogonal distance regression and assuming that all iron in the DN somata was bound to neuromelanin [53]. The alternative assumption of a homogeneous distribution of ferritin-bound iron also within DN somata resulted in a somewhat higher susceptibility value of $\chi_\rho = (3.8 \pm 0.3) \times 10^{-6}$ m^3/kg (for a detailed description, see Appendix E and Fig. 11). The Pearson correlation coefficient between cell magnetic moments and iron concentration for data generated using the first assumption was higher ($r = 0.86$) than using the second assumption ($r = 0.71$), suggesting that the first assumption was a better explanation of the data.

C. Impact of nonspherical cells

Next, we estimated the impact of the nonsphericity of NM clusters in DN soma. Their shapes deviate from the idealized spheres and may induce magnetic-field perturbations deviating from the dipole field, with contributions from higher-order multipole moments. To minimize the effect of those moments on the fit results, we excluded the 27 voxels around a DN center of mass from the fit. After excluding these voxels, the smallness parameter $(r_{\mathrm{NM}}/r)^2$ (for a full discussion, see Appendix B) for the considered

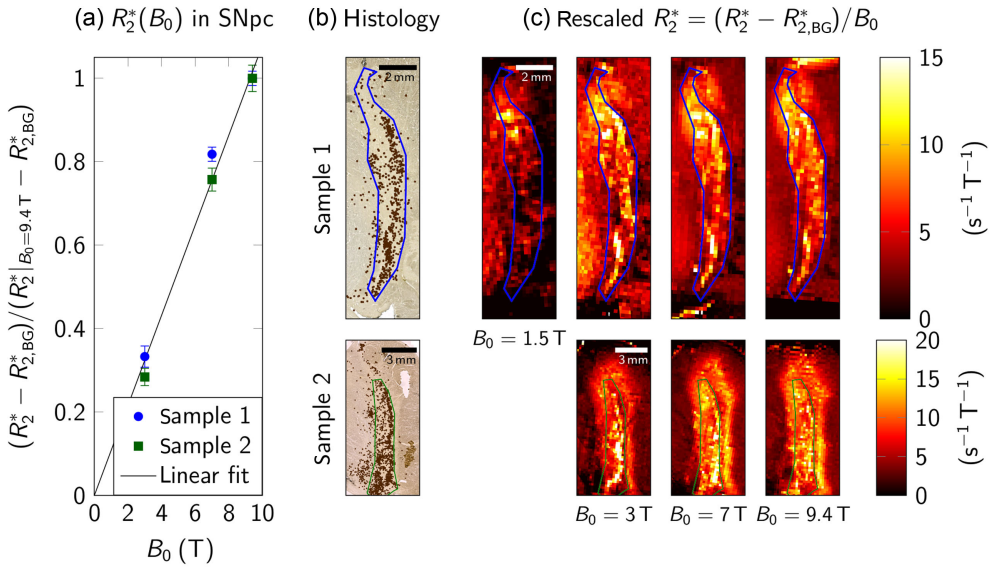

FIG. 8. The B_0-dependent contribution to R_2^* scaled approximately linearly in a DN-rich region in the SNpc. (a) We evaluated the scaling of R_2^* by fitting the model in Eq. (17) to R_2^* maps acquired at B_0 from 3 to 9 T, which resulted in $A = (0.108 \pm 0.002)$ T^{-1} and $R_{2,BG}^* = (22 \pm 2)$ s^{-1}. R_2^* at 1.5 T did not follow a linear scaling (c); hence, it was excluded from the fit. (b) Unstained sections show pigmented DN (enlarged), which were used to define the DN-rich regions of interest evaluated in (a) (sample 1, top row, blue; sample 2, bottom row, green). (c) We rescaled quantitative R_2^* maps estimated at $B_0 = 1.5$ to 9.4 T by first subtracting the B_0-independent rate $R_{2,BG}^*$ determined in (a) and second dividing the maps by the respective B_0. The resulting rescaled R_2^* maps looked very similar across B_0-field strengths between 3 and 9.4 T and showed similarly shaped regions of increased R_2^* rates. A similar color of the maps suggests that the linear rescaling effectively removed the changes between the maps. The R_2^* map at 1.5 T did not show similar contrast features as the other maps and was hence disregarded in the linear fit in (a).

voxel, which was closest to the center, was $14/(2 \times 22)^2 \approx 10\%$, using the MRI microscopy voxel size of 22 μm. Hence, the maximum expected quadrupole effect in the considered voxels closest to the DN was already quite small.

To corroborate this rationale, we tested the stability of our fit with nonspherical neurons numerically as described in the Appendix C. We used a histologically more realistic DN geometry: cones. A linear fit of the dependency of the estimated on the true dipole moment quantified the ratio of estimated mass susceptibilities for ten collections of 23 cones, matching the number of evaluated DNs. The linear fits resulted virtually in the identity line [$\mu_{fit} = (1.00 \pm 0.01)\mu_{true} - (0.00 \pm 0.03)$, mean ± standard deviation across collections], indicating no bias of our susceptibility estimate and a relative susceptibility uncertainty of 1%. Hence, the cone geometry of DNs did not change our susceptibility estimate, and we expected only a minor error in our susceptibility estimate due to the nonsphericity of DNs.

D. Extrapolation to clinical magnetic-field strengths

Having determined χ_ρ at a field strength of $B_0 = 9.4$ T, we needed to understand its scaling behavior with B_0 to extrapolate the parameter to clinical field strengths (1.5 to 7 T). Fitting the model in Eq. (17) to R_2^* maps in the SNpc revealed that $R_{2,iron}^*$ scales approximately linearly with B_0 from 3 to 9.4 T [Fig. 8(a)], which was also reflected in similar contrast features in rescaled R_2^* maps [Fig. 8(c)]. At 1.5 T, we did not observe a linear behavior, and the DN-induced contrast features disappeared. Thus, we excluded these data from the model fit [Fig. 8(c)] and could not quantify the susceptibility of iron in NM at this field strength.

These results were supported by the Monte Carlo simulation of the GE decay for a representative voxel in nigrosome 1 (Fig. 12). For the case of postmortem, formalin-fixed tissue, the static dephasing approximation for iron-induced relaxation held well for magnetic-field strengths $B_0 \geq 3$ T (R_2^* difference between static dephasing prediction and Monte Carlo simulations was less than 10%). Note that the simulation accounted for both neuromelanin- and ferritin-bound iron; hence, the static dephasing regime was a good description of the entire iron-induced GE signal decay. For 1.5 T, we observed a substantial difference of the R_2^* rates (more than 20%) predicted by the static dephasing and Monte Carlo simulations, indicating non-negligible deviation from the static dephasing regime. This deviation may explain the difference in the SNpc contrast between R_2^* maps at 1.5 T and higher fields. Combining these results with our assumptions (Sec. III I), the susceptibility of iron in NM is thus approximately the same at B_0-field strengths from 3 to 9.4 T.

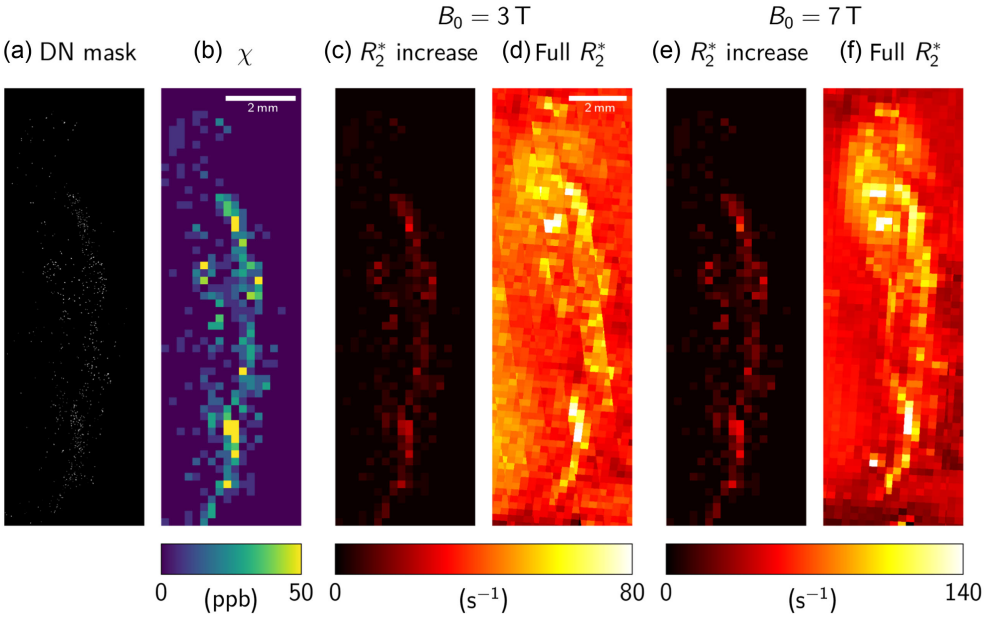

FIG. 9. Predictions of effective transverse relaxation rate R_2^* and volume susceptibility χ at clinical field strengths $B_0 = 3$ and 7 T based on histological DN somata maps and our estimate of χ_ρ (Fig. 7) for sample 1. (a) DN somata masks were obtained by segmenting pigmented NM clusters on unstained histological sections. (b) B_0-independent χ maps showed changes due to DNs within the sensitivity limits of state-of-the-art quantitative susceptibility mapping techniques [58]. (c),(e) R_2^* rates induced by DN somata, estimated from DN masks (a) using Eq. (16) at $B_0 = 3$ T (c) and 7 T (e) showed rate increases in DN-rich areas within the sensitivity limits of state-of-the-art quantitative R_2^* mapping approaches [59]. (d),(f) Experimentally obtained R_2^* maps at $B_0 = 3$ T (d) and 7 T (f) showed areas of increased relaxation rates corresponding highly to areas of high DN density.

While we estimated that the susceptibility of iron in neuromelanin is the same for B_0 from 3 to 9.4 T, this extrapolation introduced additional uncertainty. Static dephasing theory predicts a similar scaling with B_0 of the DN soma magnetic moment, which is proportional to χ_ρ, and $R_{2,\mathrm{iron}}^*$ in the DN-rich SNpc [36]. Thus, we interpreted the standard deviations of the model of $R_{2,\mathrm{iron}}^*$ [Eq. (17), Fig. 8(a)] as the relative errors of the susceptibility estimates at 3 and 7 T, which were 22% and 7%, respectively. The adapted uncertainties of χ_ρ at clinical field strength were $\chi_\rho(B_0 = 3\ \mathrm{T}) = (3.2 \pm 0.8)\ \mathrm{ppb}/(\mu\mathrm{g}/\mathrm{g})$ and $\chi_\rho(B_0 = 7\ \mathrm{T}) = (3.2 \pm 0.3)\ \mathrm{ppb}/(\mu\mathrm{g}/\mathrm{g})$ estimated assuming independent uncertainties.

We used the extrapolation of χ_ρ to estimate the effect of DN somata on quantitative MRI parameters at clinical field strengths (Fig. 9). Estimates based on histological DN somata masks [Fig. 9(a)] maps of volume susceptibility χ [Fig. 9(b)] and R_2^* [Figs. 9(c) and 9(e)] corresponded well to patterns observed on experimentally obtained R_2^* maps. The predicted χ and R_2^* maps showed alterations in DN-rich areas within the range of current *in vivo* quantitative MRI approaches [Figs. 9(b), 9(c), and 9(e)]. These results indicated that assessing iron concentration in DN somata *in vivo* is within reach of conventional MRI scanners.

For a clinical translation of our results, the increased diffusion coefficient *in vivo* limits the applicability of the static dephasing approximation to ultrahigh magnetic fields. Monte Carlo simulations of the GE decay for *in vivo* conditions indicate that the static dephasing approximation used to predict R_2^* rates here is inaccurate at $B_0 \leq 3$ T [Fig. 12(b), bottom row]. Thus, ultrahigh-field MRI at $B_0 \geq 7$ T appears as the method of choice to characterize DN iron accumulation *in vivo*. Translation of the proposed approach to lower fields requires more complex models of effective transverse relaxation accounting for diffusion. However, even complex models are in reach with increasing computing power.

V. DISCUSSION

A. New method for in-cell magnetometry of metals

We propose a novel method for in-cell magnetometry of paramagnetic metals. We developed a model that explained the signal perturbation in multiecho gradient-echo MR images by metal-rich cells such as neuromelanin-rich DN somata (Figs. 2 and 3). We quantified the magnetic moment of the DN somata by fitting this model to complex-valued MRI microscopy MEGE data (Fig. 4). After matching individual DN somata in optical microscopy and MRI microscopy, we quantified the total DN iron load in 3D using XRF and PIXE (Figs. 5, 6, and 10). Combining the measurements of the DN iron load and DN magnetic moment, we estimated the magnetic mass susceptibility of neuromelanin-bound iron to

be $\chi_\rho = (2.98 \pm 0.19) \times 10^{-6}$ m^3/kg (Fig. 7). From the experimentally observed linear scaling of the magnetic moment of DN somata with static magnetic-field strength B_0 from 3 to 9.4 T, we concluded that in this magnetic-field range the susceptibility does not depend on magnetic-field strength and generalizes to MRI scanners with field strengths above or equal to 3 T, which become increasingly clinically available.

Our method offers a remarkable advantage in single-cell detection, providing high absolute sensitivity capable of detecting picograms of paramagnetic metal per cell. This sensitivity exceeds that of microcoil electron paramagnetic resonance (EPR) by 2 orders of magnitude [60], is comparable to the absolute sensitivity achieved by diamond magnetometry [61], and lower than the absolute sensitivity achievable with state-of-the-art microscopic SQUID magnetometry [62]. Remarkably, our method enables three-dimensional imaging of macroscopic volumes, allowing for the mapping of large populations of thousands of cells and encompassing entire organs or brain nuclei. Notably, our technique operates at room temperature and can be applied to fully hydrated tissue samples, unlike microSQUID magnetometry and microEPR, which require cryogenic temperatures and offer only microscopic volume coverage. While diamond magnetometry can also be performed at room temperature, its sensitivity is limited to two-dimensional sections. Therefore, our method stands out by uniquely combining single-cell sensitivity, large volume coverage, and the ability to operate under physiological conditions.

B. New insights into brain iron biochemistry

We applied the newly developed method to measure the magnetic susceptibility of neuromelanin-bound iron directly in dopaminergic neurons in the human substantia nigra without extracting the neurons from the tissue. The magnetic mass susceptibility of neuromelanin-bound iron was found to be $\chi_\rho = (2.98 \pm 0.19) \times 10^{-6}$ m^3/kg (Fig. 7). It is about 2.5 × higher than the susceptibility of iron bound in the iron-storage protein ferritin's, which stores the majority of iron in most biological cells including neurons [41]. The similar order of magnitude of χ_ρ and $\chi_{\rho,\mathrm{FT}} = 1.24 \times 10^{-6}$ m^3/kg [41] corroborated the plausibility of the value of χ_ρ we estimated. However, the large factor between the two values enables valuable insights to be inferred regarding the specific form of iron binding in dopaminergic neurons.

Our findings indicated that most iron in neuromelanin is bound to the mononuclear site with low binding affinity. Two iron-binding sites in neuromelanin were proposed: a low-affinity, mononuclear site and a high-affinity, multinuclear site [9,11] [Fig. 2(c)]. The mononuclear site contains isolated iron ions with spin 5/2, and its magnetism is described by Curie's law, resulting in a field-independent mesoscopic susceptibility per iron load of $\chi_{\rho,\mathrm{mononuclear}} = 3.03 \times 10^{-6}$ m^3/kg [10]. As the multinuclear site was suggested to contain a ferrihydrite crystal core similar to that of the ferritin [11], we assumed here that iron in this binding site has a similar susceptibility of $\chi_{\rho,\mathrm{multinuclear}} \approx \chi_{\rho,\mathrm{FT}} = 1.24 \times 10^{-6}$ m^3/kg [41]. The susceptibility χ_ρ we determined is equal to the susceptibility of mononuclear site, within the experimental error. However, χ_ρ differs by a factor of approximately 2.5 from the susceptibility of iron in the multinuclear binding site. The B_0 independence of χ_ρ is expected for a monoatomic paramagnetic site, further underscoring its plausibility.

The iron stored in the lower affinity binding site is suggested to have higher neurotoxicity since it is easier released into the cytosol where it may induce oxidative stress [15,63]. The dominance of low-affinity bound iron found in this study may indicate a higher toxicity of iron in dopaminergic neurons as has been previously suggested. Thus, in-cell magnetometry provides valuable insight into the iron-binding form directly inside the cell.

C. New link between macroscopic MRI measures and cellular iron loads

The key advantage of our method is its applicability at room temperature and on fully hydrated tissue, allowing the magnetic susceptibility values obtained to accurately represent those found *in vivo*. Consequently, when combined with the proposed biophysical model, these obtained values establish a novel quantitative link between macroscopic *in vivo* MRI measures of brain iron and microscopic cellular iron distribution. Information about dopaminergic cell density and cellular iron load can be extracted from effective transverse relaxation rates, which can be acquired using clinically available MRI scanners.

Moreover, the large difference between the magnetic susceptibility of iron bound in ferritin and neuromelanin found in our study has important implications for MRI-based methods of iron quantification. The difference means that the sensitivity of MRI to iron stored in different chemical forms strongly differs. In the static dephasing regime, the 2.5-fold difference translates directly to a 2.5-fold-higher sensitivity of the iron-sensitive MRI parameters R_2^* and susceptibility to iron bound to neuromelanin than to iron bound to ferritin [Eq. (16)]. As iron in DN, somata comprises only between 10% and 20% of the total iron in the substantia nigra pars compacta [2,10], this increased sensitivity is pivotal for the dominant role of DN somata in effective transverse relaxation at clinical field strength. Conversely, this large difference of iron magnetic susceptibilities in the two most abundant forms (neuromelanin and ferritin) calls into question the applicability of simplified MRI contrast models, which use a single proportionality constant to relate R_2^* rates and QSM values to tissue iron concentrations [31,64,65]. Our results show that it is an oversimplification to treat iron in the human substantia

nigra as a single tissue component when interpreting iron-sensitive MRI contrasts. Our results determine an important parameter for biophysical modeling of transverse relaxation in the substantia nigra, which is required to quantify DN iron *in vivo* [10].

D. Detection of dopaminergic neurons with MRI microscopy

To the best of our knowledge, we reported the first direct depiction of neurons using MRI without exogenous contrast agents. While the traces of iron-rich glial cells have been visualized in MRI before [35], usually neurons are MR invisible as they do not contain sufficient iron or other sources of MRI relaxation. Dopaminergic neurons are a rare exception, rendering MRI a promising tool for 3D DN histology, without the need of time-consuming and costly tissue clearing [66]. Ultrahigh-resolution and ultrahigh-field postmortem MRI enables one to study changes of DN populations and their iron content during healthy aging [15] and in Parkinson's disease [7] for large sample sizes, overcoming limitations of histological approaches.

As far as we are aware, our work was the first application of superresolution localization microscopy to QSM on single, spatially separate cells. The idea of localization microscopy is to use the knowledge of the point-spread function of the signal from isolated emitters (here, iron-rich DN somata) to deconvolve the acquired signal and retrieve information on scales below the imaging resolution. While in the case of QSM, the zero crossings of the dipole kernel complicate the application of a deconvolution kernel, our approach circumvented this problem by relying solely on the forward model. Assuming a simple geometry of the DN soma, our method revealed the center of mass of the DN somata with subvoxel resolution of about a micrometer, as well as its magnetic moment, which for the present study is of greater interest.

E. Toward *in vivo* MRI mapping of dopaminergic neurons integrity

The established quantitative link between macroscopic and microscopic quantitative MRI (qMRI) parameters and the density and iron load of dopaminergic neurons paves the way for noninvasive assessment of their integrity using clinical MRI scanners. This breakthrough has the potential to enable early detection of neurodegeneration in PD before the onset of motor symptoms. Our model predicts that the effective transverse relaxation rate in nigrosome 1 within the substantia nigra exhibits a linear relationship with the cellular density and iron load of dopaminergic cells, serving as a potential biomarker for assessing cell integrity. However, before clinical translation can be achieved, several challenges must be addressed. First, the magnetometry measurement and biophysical model conducted in this study in the tissue of aged donors need to be extended to cover the entire adult lifespan and include PD patient tissue.

Second, the application of the method *in vivo* will need an ultrahigh-resolution qMRI acquisition at ultrahigh-field strengths. Fortunately, recent FDA approval of 7-T technology coupled with breakthroughs in image acquisition, reconstruction, and prospective motion correction techniques [16] has enabled submillimeter resolution quantitative MRI at 7 T [67,68], narrowing the gap to the *in vivo* application of our results.

Third, any new imaging biomarker needs to be tested in a clinical trial. qMRI markers have already generated significant interest in radiology and neurology since the advantage of improved interpretability and comparability are recognized [69] and clinical translation is ongoing (e.g., nogo inhibition in spinal cord injury).

F. Methodological considerations

Our results allow us to assess the optimum B_0-field strength for imaging the substantia nigra pars compacta. R_2^* maps at B_0 from 3 to 9.4 T showed similar features within SN. This implies that MRI at 3 T, which is clinically widely available, is in principle sensitive to the contrast of the rich substructure within the SNpc. Nevertheless, the increased contrast-to-noise at higher B_0 fields is beneficial to achieve higher spatial resolutions. Furthermore, the contribution of iron in DNs to R_2^* is most effective in the static dephasing regime, which applies *in vivo* for $B_0 > 3$ T (Fig. 12). Hence, MRI at 7 T is most promising for SNpc mapping, especially as it is becoming more and more clinically available.

To improve the reliability of our susceptibility measures, we quantified cellular iron concentrations with two independent methods: proton-induced x-ray emission [49,70–72] and x-ray fluorescence [50]. While both methods quantify iron from first physical principles and are widely used in material sciences, fewer studies apply them to quantify elements in postmortem tissue specimens. To the knowledge of the authors, no systematic comparison between PIXE and XRF elemental quantification in postmortem tissue has been performed yet.

In this study, cross-referencing both methods showed a high correspondence between the iron load of DNs, which validates our cellular iron concentration measurement. These results provide a reliable foundation for future studies of cellular metal accumulation and in-cell magnetometry.

G. Limitations and modeling assumptions

Among the limitations of our study was the small sample size of two examined postmortem specimens and the limited number of 23 neurons that were included in the analysis. Furthermore, a possible change of MRI contrast mechanisms in the substantia nigra after death may limit the translation of our results to *in vivo* MRI. During histological processing, iron may be washed out

of neuromelanin, leading to the overestimation of iron's susceptibility.

Because of the presence of more than one iron-binding site in neuromelanin, the value of χ_ρ may change during aging and in pathology. Neuromelanin's mesoscopic susceptibility per iron load agreed well between the two specimens we examined, indicating a similar distribution of iron between the two proposed binding sites of iron in the neuromelanin in healthy aging [15]. Future research should address the question of whether this value is preserved in Parkinson's disease or whether the hypothesized higher loading of the low-affinity, isolated iron-binding site alters χ_ρ [11].

In the translation of our results to *in vivo* MRI, several effects have to be considered. The increased temperature decreases the susceptibility. Assuming a paramagnetic behavior, we estimated this effect to reduce the susceptibility by 5% using Curie's law.

VI. CONCLUSION

We developed a new method for in-cell magnetometry of paramagnetic metals, combining superresolution MRI microscopy and biophysical modeling with 3D quantitative iron histology. The method goes beyond the state-of-the-art methodology in metallomics by providing unbiased values of magnetic susceptibility measured directly in single cells and in large cell ensembles.

We applied this method to study iron bound to neuromelanin in dopaminergic neurons in human substantia nigra pars compacta. We estimated that the mass susceptibility of neuromelanin-bound iron is $(2.98 \pm 0.19) \times 10^{-6}$ m^3/kg. This value is very close to the susceptibility of monoatomic iron with spin $5/2$, suggesting that the majority of iron in neuromelanin may be bound in the low-affinity binding site, which is potentially neurotoxic.

Moreover, the obtained susceptibility values provide the essential parameter for linking *in vivo* measurements of brain iron using clinical MRI scanners to iron concentrations in dopaminergic neurons. Therefore, our results constitute an important step toward a quantitative biomarker of iron in dopaminergic neurons, which could shed light on the link of iron accumulation and neuronal depletion in Parkinson's disease with high-throughput 3D quantitative iron histology.

The presented method can be applied to other cell types and other paramagnetic metals to study the physiology of metals in biological cells and their potential for novel imaging biomarkers.

ACKNOWLEDGMENTS

M. B. has received funding from the International Max Planck Research School on Neuroscience of Communication: Function, Structure, and Plasticity. N. W. has received funding from the European Union's Horizon 2020 research and innovation program under Grant Agreement No. 681094. The research leading to these results has received funding from the European Research Council under the European Union's Seventh Framework Programme (FP7/2007-2013), ERC Grant Agreement No. 616905. Work was supported by the EU Joint Programme Neurodegenerative Disease Research, and the project was funded by the Federal Ministry of Education and Research under support code 01ED2210. Aspects of this work were supported by funding from the German Research Foundation (DFG Priority Program 2041 Computational Connectomics, Grants No. MO 2249/31, No. WE 5046/4-2, and No. KI 1337/2-2) and the Alzheimer Forschungsinitiative e.V. (AFI No. 18072) to M. M. The Max Planck Institute for Human Cognitive and Brain Sciences and Wellcome Centre for Human Neuroimaging have institutional research agreements with Siemens Healthcare. We acknowledge DESY (Hamburg, Germany), a member of the Helmholtz Association HGF, for providing the experimental facilities, including the beamtime allocated for Proposal No. I-20211534, at the microprobe beamline P06 at PETRA III. This research was supported in part through the Maxwell computational resources operated at Deutsches Elektronen-Synchrotron DESY, Hamburg, Germany.

The Max Planck Institute for Human Cognitive and Brain Sciences has an institutional research agreement with Siemens Healthcare. N. W. was a speaker at an event organized by Siemens Healthcare and was reimbursed for the travel expenses.

APPENDIX A: IMPACT OF NONSPHERICITY OF NEURONAL SOMATA

Consider a compact but not necessarily spherical perturber of magnetic field such as an iron-loaded cell. Consider for simplicity the case when its magnetic susceptibility χ_v is constant within the cell volume. The spatial distribution of magnetic susceptibility is then $\chi_v v(\mathbf{r})$, where $v(\mathbf{r})$ is the indicator function of the cell $v(\mathbf{r}) = 1$ inside the cell, otherwise zero. When exposed to the main field B_0 of an MR device, such a cell perturbs the local Larmor frequency, adding the sum of all infinitesimally small dipole moments $(B_0/\mu_0)d^3\mathbf{r}\chi_v$ in a continuous version of Eq. (7),

$$\omega(\mathbf{r}) = \delta\omega \int d^3\mathbf{r}_0 v(\mathbf{r}_0) Y(\mathbf{r} - \mathbf{r}_0). \tag{A1}$$

Here, $\mathbf{r}$ points from the cell center of mass to an arbitrary point outside the cell, $\delta\omega = -\gamma B_0 \chi_v/3$ is the characteristic Larmor frequency, and the integration over the whole space is effectively limited to the cell volume by the factor $v(\mathbf{r})$. The elementary dipole field takes the form

$$Y(\mathbf{r}) = \frac{3n_z^2 - 1}{r^3} = \frac{\partial^2}{\partial z^2}\frac{1}{r}, \tag{A2}$$

where z is the third component of $\mathbf{r}$ as defined by the direction of the main field and $n_z = z/r$. The last expression connects the dipole field to the Coulomb potential.

Our goal is to find the Larmor frequency field on the distance $\mathbf{r}$ that is much larger than the cell dimensions, $r \gg \varrho$. We substitute the last form of Eq. (A2) in Eq. (A1) and perform the Taylor expansion in $\mathbf{r}$, which leads to the standard multipole expansion. To simplify calculations, we use the last form of the dipole field in Eq. (A2). This gives

$$\omega(r) = \delta\omega\frac{\partial^2}{\partial z^2}\int d^3\mathbf{r}v(\mathbf{r})\left[1 - r_a\frac{\partial}{\partial r_a} + \frac{1}{2}r_a r_b\frac{\partial^2}{\partial r_a \partial r_b} + \ldots\right]\frac{1}{r}, \tag{A3}$$

where the indices a and b label the three components of corresponding vectors, and the Einstein's convention about the summation over the repeating indices is implied. Analyzing this expression term by term, the integration in the first term gives the cell volume. Thus, the leading term in the far field coincides with the pure dipole field (obtained by the double differentiation of $1/r$). The absence of any correction to this field is the property of a uniformly polarized sphere, which justifies the approximation of the spherical cell shape for the far field.

The second term in the brackets, which is of the first order in r_a, gives zero upon integration according to the definition of the center of mass.

The third term in Eq. (A3) is the correction we are looking for. It is convenient to replace $r_a r_b$ with $r_a r_b - r^2\delta_{ab}/3$. The delta symbol does not change the expression because it adds zero,

$$\delta_{ab}\frac{\partial^2}{\partial r_a \partial r_b}\frac{1}{r} = \nabla^2\frac{1}{r} = 0, \qquad R \neq 0. \tag{A4}$$

With this addition, the integration gives the standard quadrupole of the cell shape,

$$Q_{ab} = \int d^3\mathbf{r}v(\mathbf{r})\left[r_a r_b - \frac{1}{3}r^2\delta_{ab}\right]. \tag{A5}$$

The correction to the field from the nonspherical cell shape is thus

$$\Delta\omega(\mathbf{r}) = \frac{1}{2}\delta\omega Q_{ab}\frac{\partial^2}{\partial z^2}\frac{\partial^2}{\partial r_a \partial r_b}\frac{1}{r}. \tag{A6}$$

In summary, the quadrupole component in the cell shape adds a field with up to the fourth-order multipole pattern (octopole) in the induced Larmor frequency. This component decreases as $1/r^5$. At large distances from the cell, it is smaller compared to the dipole field proportional to $1/r^3$. The dimensionless smallness parameter can be estimated as $(\varrho/r)^2$, where ϱ is the characteristic cell radius. Further, the effect of $\Delta\omega(\mathbf{r})$ can be reduced in fitting due to the higher order of the involved spherical harmonics $l = 4$ compared to $l = 2$ of the dipole field.

APPENDIX B: NUMERICAL EVALUATION OF THE IMPACT OF NONSPHERICITY OF NEURONAL SOMATA

We numerically evaluated the effect of soma nonsphericity on the susceptibility quantification. To this end, we generated synthetic DN susceptibility maps with a DN geometry that more closely resembles the appearance of the neurons on histological tissue sections: cones. We created maps of randomly oriented cone-shaped susceptibility inclusions with the same volume as the spherical model described in Sec. III D. For each cone-shaped inclusion, we randomly selected the following parameters from the appropriate ranges: the cone magnetic moment from 90 to 550 mA μm^2, the opening angle of the cone from 25° to 65° (matching opening angles of neuromelanin domains on unstained histological tissue sections), and the displacement of the cone within a voxel along each spatial dimension from −10 to 10 μm. We created ten collections of 23 cone susceptibility maps corresponding to the number of experimentally evaluated DNs.

From these susceptibility maps, we generated MEGE data using Eq. (15) with the experimental parameters of the 9.4-T MRI microscopy (see Table I). In Eq. (15), we used the following background tissue parameters: $R_2 = 0.8\,\mathrm{ms}^{-1}$, which was approximately the average R_2 rate obtained from the DN susceptibility quantification, and $\phi_{\mathrm{BG}} = \omega_{\mathrm{BG}} = 0$, which removed a global linear phase factor that did not impact the results substantially.

Next, we applied the magnetic moment quantification described in Sec. III D to these synthetic data to estimate the magnetic moment of the cone-shaped DNs. For each collection of 23 cone-shaped DNs, we plotted the dependency of estimated dipole moments on the true dipole moments and performed a linear fit. The slope of the linear fit quantified the ratio of the mass susceptibilities estimated for cones and spheres. Averaging the slope over the cone collections indicated whether cone-shaped, nonspherical DNs introduced a bias into the mass susceptibility estimate.

APPENDIX C: ASSESSING THE ACCURACY OF CELLULAR IRON MEASUREMENTS WITH AN INDEPENDENT METHOD

To quantify the precision of cellular iron masses determined using PIXE, we compared them to measurements by the independent XRF method. We quantified the iron mass for the set of 20 randomly selected neurons in sample 1 (Fig. 10). The iron masses measured by both methods

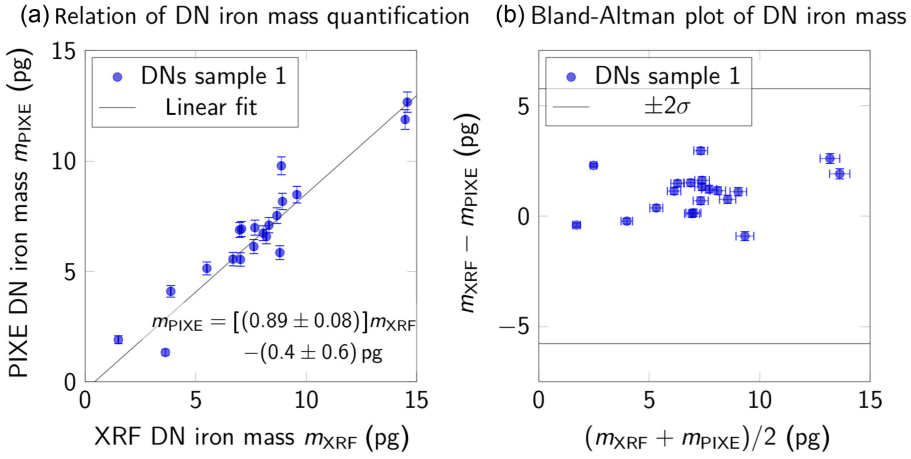

FIG. 10. Relation of iron mass in 20 randomly selected DNs quantified in sample 1 using XRF and PIXE. (a) DN iron mass quantified with XRF and PIXE showed high correspondence. A linear fit to the data was close to the identity line (parameters given on plot). (b) Bland-Altman plot of DN iron masses shows high accuracy of iron quantification using PIXE and XRF, with deviations well below twice the standard deviation of the iron masses. The PIXE DN iron mass had a bias toward lower values compared to the XRF DN iron mass.

agreed well, with the accuracy of 10% as indicated by a slope of a linear function fitted to the experimental data.

APPENDIX D: EVALUATING THE IMPACT OF THE IRON-BINDING FORM IN DOPAMINERGIC NEURONS ON THE MASS SUSCEPTIBILITY OF NEUROMELANIN

Here, we evaluate the susceptibility of neuromelanin-bound iron in the case of a homogeneous distribution of ferritin-bound iron. In the main text, we determined the mass susceptibility of neuromelanin-bound iron assuming that iron in neuromelanin domains is exclusively bound to neuromelanin, not to ferritin. As PIXE and XRF are not sensitive to the iron-binding form (neuromelanin or ferritin), it was not possible to verify this assumption experimentally. Hence, here we analyze the consequences of assuming the opposite limiting case: a homogeneous distribution of ferritin-bound iron also within neuromelanin domains. In this case, we predict a somewhat higher mass susceptibility of neuromelanin-bound iron (Fig. 11). However, our model explains the experimental data worse compared to the assumption followed in the manuscript (Fig. 7). Hence, we rejected this assumption in favor of an exclusive binding of iron to neuromelanin in dopaminergic neurons.

APPENDIX E: APPLICABILITY OF STATIC DEPHASING IN MRI RELAXOMETRY

Here, we analyze the applicability of the static dephasing approximation to the GE signal decay at various B_0 under *in vivo* and postmortem conditions. If the static dephasing approximation is applicable, the R_2^* rate induced by susceptibility inclusions as iron-rich dopaminergic neurons scales linearly with B_0. This linear scaling was used to extrapolate the mass susceptibility of neuromelanin-bound iron to lower field strengths (Sec. III I) where MRI microscopy was challenging. Moreover, in the case of static dephasing, the iron load and density of dopaminergic

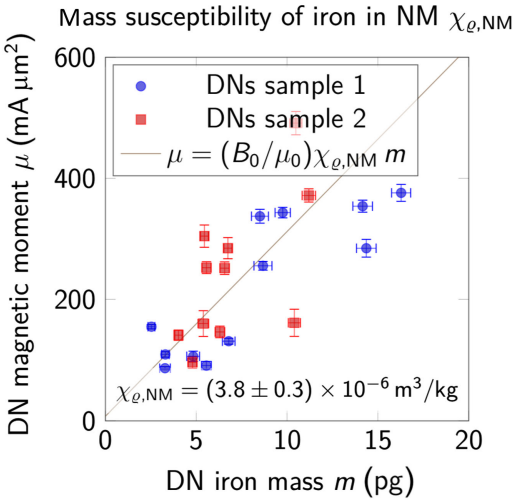

FIG. 11. Determining the mass susceptibility of iron bound to neuromelanin in dopaminergic neurons χ_ρ assuming a homogeneous distribution of ferritin-bound iron also within dopaminergic neurons. Each dot in the scatter plot represents one DN soma with its magnetic moment on the vertical axis and its iron mass on the horizontal axis. Fitting the experimental data with a straight line (solid line) using an orthogonal distance regression [53], we estimated $\chi_\rho = (3.8 \pm 0.3) \times 10^{-6}$ m^3/kg. This susceptibility value was increased by 34% compared to the value determined for the assumption that all iron within the neuromelanin domains of dopaminergic neurons is stored in neuromelanin (Fig. 7).

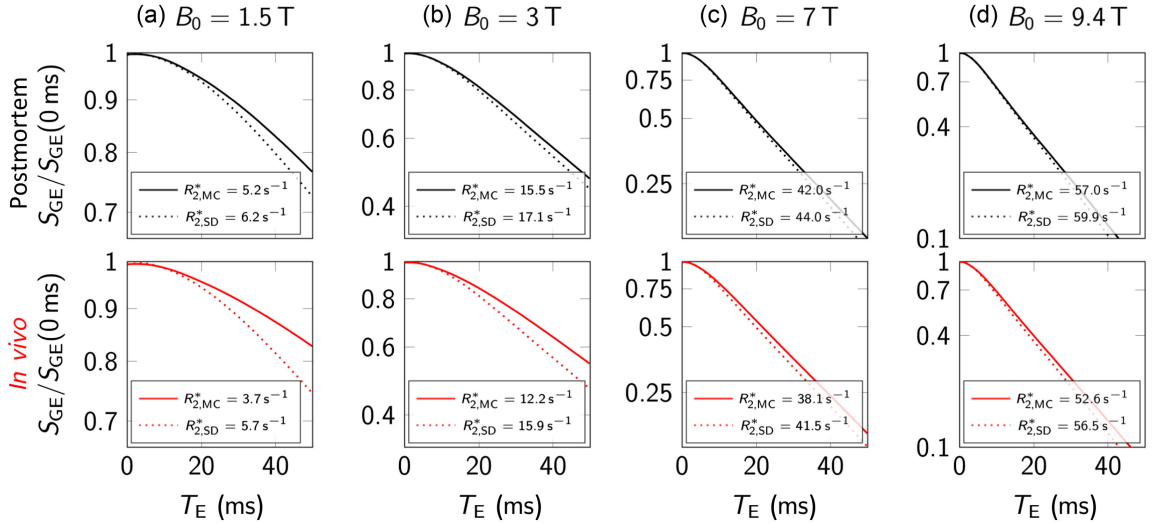

FIG. 12. Applicability of the static dephasing approximation for gradient-echo decays in nigrosome 1 postmortem and *in vivo* at varying B_0. We assessed the applicability of the SD approximation, i.e., negligible water diffusion effects, by comparing decays predicted for a representative voxel in nigrosome 1 using this approximation (dashed lines) to those predicted by a Monte Carlo simulation (MC) accounting for water diffusion (solid lines), as described previously [10]. In the Monte Carlo simulations, we assumed diffusion coefficients of 0.3 $\mu m^2/ms$ in postmortem, formalin-fixed tissue and 1 $\mu m^2/ms$ *in vivo*. We obtained R_2^* rates for the simulated decays by fitting an exponential decay function to the simulated decays sampled at equally spaced echo times T_E ranging from 4 to 41 ms, as described before [10]. For the postmortem case (top row), high field strengths of $B_0 \geq 3$ T [(b)–(d)] showed a good agreement between static dephasing and Monte Carlo simulation predictions (less than 10% difference between R_2^* values), while R_2^* values differed by more than 20% for $B_0 = 1.5$ T [(a)]. For the *in vivo* case (bottom row), ultrahigh-field strengths of 7 and 9.4 T [(c),(d)] showed high correspondence between static dephasing and Monte Carlo predictions (less than 10% difference between R_2^* values). Field strengths of 1.5 and 3 T [(a),(b)] showed higher deviations between the two predictions with R_2^* values differing by more than 30%. Thus, the static dephasing approximation is suitable for fields equal to or higher than 3 T in postmortem tissue and equal to or higher than 7 T *in vivo*.

neurons can be inferred from R_2^* measurements, based on Eq. (16), providing a promising avenue for measuring their integrity *in vivo* [10].

To test the applicability of the static dephasing approximation, we employed a previously published numerical model of the GE signal decay in an area in the substantia nigra densely populated with dopaminergic neurons, nigrosome 1 [10]. While we refer to the original publication [10] for a detailed description of the model, we briefly summarize its main aspects here. The model is based on a microscopic, quantitative 3D map of iron distribution in human nigrosome 1 within a volume of the size of a typical MRI voxel. This map was obtained using quantitative iron histology, combining PIXE and classical histological stains for iron. The iron-induced microscopic susceptibility heterogeneity within the voxel was estimated by scaling iron concentration maps, with the mass susceptibilities of neuromelanin- and ferritin-bound iron. For this estimate, we replaced the susceptibility of neuromelanin-bound iron in Ref. [10] with the value obtained in the present study. The published model estimates the GE signal decay using two approaches: numerically using Monte Carlo simulations and analytically using the static dephasing approximation. The Monte Carlo simulation tracks the phases of many water spin packets diffusing through the 3D susceptibility map. The GE signal decay is estimated by averaging the phase factors of all spin packets at each time point. For the case of static dephasing, the GE signal decay was estimated as the Fourier transform of the Larmor frequency histogram derived from the 3D susceptibility map. For both cases, R_2^* rates were estimated by fitting an exponential function $\exp(-R_2^* T_E)$ to the signal predicted at experimentally realistic echo times T_E. We considered the static dephasing approximation as accurate if the difference between the R_2^* rates predicted using Monte Carlo simulations and static dephasing theory was lower than 10%.

The simulations using the described model demonstrated that the static dephasing approximation was applicable for $B_0 \geq 3$ T in postmortem tissue and for $B_0 \geq 7$ T *in vivo* (Fig. 12). In postmortem tissue, the differences between R_2^* rates predicted by static dephasing theory and by Monte Carlo simulations were 21% for $B_0 = 1.5$ T, 9% for $B_0 = 3$ T, 4% for $B_0 = 7$ T, and 2% for $B_0 = 9.4$ T. For *in vivo* conditions, those differences in R_2^* rates were 53% for $B_0 = 1.5$ T, 31% for $B_0 = 3$ T, 8% for $B_0 = 7$ T, and 4% for $B_0 = 9.4$ T.

[1] R. H. Holm, P. Kennepohl, and E. I. Solomon, *Structural and functional aspects of metal sites in biology*, Chem. Rev. **96**, 2239 (1996).

[2] I. Friedrich, K. Reimann, S. Jankuhn, E. Kirilina, J. Stieler, M. Sonntag, J. Meijer, N. Weiskopf, T. Reinert, T. Arendt, and M. Morawski, *Cell specific quantitative iron mapping on brain slices by immuno-PIXE in healthy elderly and Parkinsons disease*, Acta Neuropathol. Commun. **9**, 47 (2021).

[3] T. Ganz and E. Nemeth, *Hepcidin and iron homeostasis*, Biochim. Biophys. Acta **1823**, 1434 (2012).

[4] R. Franklin, J. Ma, J. Zou, Z. Guan, B. Kukoyi, P. Feng, and L. Costello, *Human zip1 is a major zinc uptake transporter for the accumulation of zinc in prostate cells*, J. Inorg. Biochem. **96**, 435 (2003).

[5] S. N. Haber and B. Knutson, *The reward circuit: Linking primate anatomy and human imaging*, Neuropsychopharmacology **35**, 4 (2010).

[6] J. D. Berke, *What does dopamine mean?*, Nat. Neurosci. **21**, 787 (2018).

[7] P. Damier, E. C. Hirsch, Y. Agid, and A. M. Graybiel, *The substantia nigra of the human brain. II. Patterns of loss of dopamine-containing neurons in Parkinson's disease*, Brain **122**, 1437 (1999).

[8] L. V. Kalia and A. E. Lang, *Parkinson's disease*, Lancet **386**, 896 (2015).

[9] D. Sulzer, C. Cassidy, G. Horga, U. J. Kang, S. Fahn, L. Casella, G. Pezzoli, J. Langley, X. P. Hu, F. A. Zucca, I. U. Isaias, and L. Zecca, *Neuromelanin detection by magnetic resonance imaging (MRI) and its promise as a biomarker for Parkinsons disease*, NPJ Parkinson's Dis. **4**, 11 (2018).

[10] M. Brammerloh, M. Morawski, I. Friedrich, T. Reinert, C. Lange, P. Pelicon, P. Vavpeti, S. Jankuhn, C. Jäger, A. Alkemade, R. Balesar, K. Pine, F. Gavriilidis, R. Trampel, E. Reimer, T. Arendt, N. Weiskopf, and E. Kirilina, *Measuring the iron content of dopaminergic neurons in substantia nigra with MRI relaxometry*, NeuroImage **239**, 118255 (2021).

[11] F. A. Zucca, J. Segura-Aguilar, E. Ferrari, P. Muoz, I. Paris, D. Sulzer, T. Sarna, L. Casella, and L. Zecca, *Interactions of iron, dopamine and neuromelanin pathways in brain aging and Parkinson's disease*, Prog. Neurobiol. **155**, 96 (2017).

[12] F. Bolzoni, S. Giraudo, L. Lopiano, B. Bergamasco, M. Fasano, and P. R. Crippa, *Magnetic investigations of human mesencephalic neuromelanin*, Biochim. Biophys. Acta **1586**, 210 (2002).

[13] K. L. Double, M. Gerlach, V. Schünemann, A. X. Trautwein, L. Zecca, M. Gallorini, M. B. H. Youdim, P. Riederer, and D. Ben-Shachar, *Iron-binding characteristics of neuromelanin of the human substantia nigra*, Biochem. Pharmacol. **66**, 489 (2003).

[14] B. A. Faucheux, M.-E. Martin, C. Beaumont, J.-J. Hauw, Y. Agid, and E. C. Hirsch, *Neuromelanin associated redox-active iron is increased in the substantia nigra of patients with Parkinson's disease*, J. Neurochem. **86**, 1142 (2003).

[15] L. Zecca, M. B. H. Youdim, P. Riederer, J. R. Connor, and R. R. Crichton, *Iron, brain ageing and neurodegenerative disorders*, Nat. Rev. Neurosci. **5**, 863 (2004).

[16] N. Weiskopf, L. J. Edwards, G. Helms, S. Mohammadi, and E. Kirilina, *Quantitative magnetic resonance imaging of brain anatomy and in vivo histology*, Nat. Rev. Phys. **3**, 570 (2021).

[17] J.-Y. Lee, A. Martin-Bastida, A. Murueta-Goyena, I. Gabilondo, N. Cuenca, P. Piccini, and B. Jeon, *Multimodal brain and retinal imaging of dopaminergic degeneration in Parkinson disease*, Nat. Rev. Neurol. **18**, 203 (2022).

[18] P. Trujillo, P. E. Summers, E. Ferrari, F. A. Zucca, M. Sturini, L. T. Mainardi, S. Cerutti, A. K. Smith, S. A. Smith, L. Zecca, and A. Costa, *Contrast mechanisms associated with neuromelanin-MRI*, Magn. Reson. Med. **78**, 1790 (2017).

[19] H. Lee, S.-Y. Baek, S. Y. Chun, J.-H. Lee, and H. Cho, *Specific visualization of neuromelanin-iron complex and ferric iron in the human post-mortem substantia nigra using MR relaxometry at 7 T*, NeuroImage **172**, 874 (2018).

[20] A. I. Blazejewska, S. T. Schwarz, A. Pitiot, M. C. Stephenson, J. Lowe, N. Bajaj, R. W. Bowtell, D. P. Auer, and P. A. Gowland, *Visualization of nigrosome 1 and its loss in PD pathoanatomical correlation and in vivo 7 T MRI*, Neurology **81**, 534 (2013).

[21] A. K. Lotfipour, S. Wharton, S. T. Schwarz, V. Gontu, A. Schäfer, A. M. Peters, R. W. Bowtell, D. P. Auer, P. A. Gowland, and N. P. Bajaj, *High resolution magnetic susceptibility mapping of the substantia nigra in Parkinson's disease*, J. Magn. Reson. Imaging **35**, 48 (2012).

[22] M. Sasaki, E. Shibata, K. Tohyama, J. Takahashi, K. Otsuka, K. Tsuchiya, S. Takahashi, S. Ehara, Y. Terayama, and A. Sakai, *Neuromelanin magnetic resonance imaging of locus ceruleus and substantia nigra in Parkinson's disease*, NeuroReport **17**, 1215 (2006).

[23] C. M. Cassidy, F. A. Zucca, R. R. Girgis, S. C. Baker, J. J. Weinstein, M. E. Sharp, C. Bellei, A. Valmadre, N. Vanegas, L. S. Kegeles, G. Brucato, U. J. Kang, D. Sulzer, L. Zecca, A. Abi-Dargham, and G. Horga, *Neuromelanin-sensitive MRI as a noninvasive proxy measure of dopamine function in the human brain*, Proc. Natl. Acad. Sci. U.S.A. **116**, 5108 (2019).

[24] E. Y. Kim, Y. H. Sung, and J. Lee, *Nigrosome 1 imaging: Technical considerations and clinical applications*, Br. J. Radiol. **92**, 20180842 (2019).

[25] K. Shmueli, J. A. de Zwart, P. van Gelderen, T.-Q. Li, S. J. Dodd, and J. H. Duyn, *Magnetic susceptibility mapping of brain tissue in vivo using MRI phase data*, Magn. Reson. Med. **62**, 1510 (2009).

[26] E. M. Haacke, S. Liu, S. Buch, W. Zheng, D. Wu, and Y. Ye, *Quantitative susceptibility mapping: Current status and future directions*, Magn. Reson. Imaging **33**, 1 (2015).

[27] B. Bilgic, A. Pfefferbaum, T. Rohlfing, E. V. Sullivan, and E. Adalsteinsson, *MRI estimates of brain iron concentration in normal aging using quantitative susceptibility mapping*, NeuroImage **59**, 2625 (2012).

[28] M. C. Keuken, P.-L. Bazin, K. Backhouse, S. Beekhuizen, L. Himmer, A. Kandola, J. J. Lafeber, L. Prochazkova, A. Trutti, A. Schäfer, R. Turner, and B. U. Forstmann, *Effects of aging on T_1, T_2^*, and QSM MRI values in the subcortex*, Brain Struct. Funct. **222**, 2487 (2017).

[29] M. J. Betts, J. Acosta-Cabronero, A. Cardenas-Blanco, P. J. Nestor, and E. Dzel, *High-resolution characterisation of the aging brain using simultaneous quantitative susceptibility mapping (QSM) and R_2* measurements at 7 T*, NeuroImage **138**, 43 (2016).

[30] G. Du, T. Liu, M. M. Lewis, L. Kong, Y. Wang, J. Connor, R. B. Mailman, and X. Huang, *Quantitative susceptibility mapping of the midbrain in Parkinson's disease*, J. Mov. Disord. **31**, 317 (2016).

[31] C. Langkammer, L. Pirpamer, S. Seiler, A. Deistung, F. Schweser, S. Franthal, N. Homayoon, P. Katschnig-Winter, M. Koegl-Wallner, T. Pendl, E. M. Stoegerer, K. Wenzel, F. Fazekas, S. Ropele, J. R. Reichenbach, R. Schmidt, and P. Schwingenschuh, *Quantitative susceptibility mapping in Parkinson's disease*, PLoS One **11**, e0162460 (2016).

[32] J.-H. Lee, S.-Y. Baek, Y. Song, S. Lim, H. Lee, M. P. Nguyen, E.-J. Kim, G. Y. Huh, S. Y. Chun, and H. Cho, *The neuromelanin-related $T2^*$ contrast in postmortem human substantia nigra with 7 T MRI*, Sci. Rep. **6**, 32647 (2016).

[33] J. P. Marques, R. Maddage, V. Mlynarik, and R. Gruetter, *On the origin of the MR image phase contrast: An in vivo MR microscopy study of the rat brain at 14.1 T*, NeuroImage **46**, 345 (2009).

[34] J. W. M. Bulte, P. C. M. van Zijl, and S. Mori, *Magnetic resonance microscopy and histology of the CNS*, Trends Biotechnol. **20**, S24 (2002).

[35] G. Nair, S. Dodd, S.-K. Ha, A. P. Koretsky, and D. S. Reich, *Ex vivo MR microscopy of a human brain with multiple sclerosis: Visualizing individual cells in tissue using intrinsic iron*, NeuroImage **223**, 117285 (2020).

[36] D. A. Yablonskiy and E. M. Haacke, *Theory of NMR signal behavior in magnetically inhomogeneous tissues: The static dephasing regime*, Magn. Reson. Med. **32**, 749 (1994).

[37] A. Alkemade, P.-L. Bazin, R. Balesar, K. Pine, E. Kirilina, H. E. Möller, R. Trampel, J. M. Kros, M. C. Keuken, R. L. A. W. Bleys, D. F. Swaab, A. Herrler, N. Weiskopf, and B. U. Forstmann, *A unified 3D map of microscopic architecture and MRI of the human brain*, Sci. Adv. **8**, eabj7892 (2022).

[38] V. G. Kiselev and D. S. Novikov, *Transverse NMR relaxation in biological tissues*, NeuroImage **182**, 149 (2018).

[39] H. C. Torrey, *Bloch equations with diffusion terms*, Phys. Rev. **104**, 563 (1956).

[40] L. J. Edwards, E. Kirilina, S. Mohammadi, and N. Weiskopf, *Microstructural imaging of human neocortex in vivo*, NeuroImage **182**, 184 (2018).

[41] J. F. Schenck, *Health and physiological effects of human exposure to whole-body four-Tesla magnetic fields during MRI*, Ann. N.Y. Acad. Sci. **649**, 285 (1992).

[42] E. M. Haacke, R. W. Brown, M. R. Thompson, and R. Venkatesan, *Magnetic Resonance Imaging: Physical Principles and Sequence Design* (Wiley, New York, 1999).

[43] J. P. Marques, J. Meineke, C. Milovic, B. Bilgic, K.-S. Chan, R. Hedouin, W. van der Zwaag, C. Langkammer, and F. Schweser, *QSM reconstruction challenge 2.0: A realistic in silico head phantom for MRI data simulation and evaluation of susceptibility mapping procedures*, Magn. Reson. Med. **86**, 526 (2021).

[44] J. Marques and R. Bowtell, *Application of a Fourier-based method for rapid calculation of field inhomogeneity due to spatial variation of magnetic susceptibility*, Concepts Magn. Reson., Part B **25**, 65 (2005).

[45] K. Eckstein, B. Dymerska, B. Bachrata, W. Bogner, K. Poljanc, S. Trattnig, and S. D. Robinson, *Computationally efficient combination of multi-channel phase data from multi-echo acquisitions (ASPIRE)*, Magn. Reson. Med. **79**, 2996 (2018).

[46] N. Weiskopf, J. Suckling, G. Williams, M. M. Correia, B. Inkster, R. Tait, C. Ooi, E. T. Bullmore, and A. Lutti, *Quantitative multi-parameter mapping of R1, PD*, MT, and $R2^*$ at 3 T: A multi-center validation*, Front. Neurosci. **7**, 95 (2013).

[47] P. Virtanen *et al.*, *SciPy1.0: Fundamental algorithms for scientific computing in PYTHON*, Nat. Methods **17**, 261 (2020).

[48] N. Barapatre, M. Morawski, T. Butz, and T. Reinert, *Trace element mapping in Parkinsonian brain by quantitative ion beam microscopy*, Nucl. Instrum. Methods Phys. Res., Sect. B **268**, 2156 (2010).

[49] M. Morawski, T. Reinert, W. Meyer-Klaucke, F. E. Wagner, W. Törger, A. Reinert, C. Jäger, G. Brückner, and T. Arendt, *Ion exchanger in the brain: Quantitative analysis of perineuronally fixed anionic binding sites suggests diffusion barriers with ion sorting properties*, Sci. Rep. **5**, 16471 (2015).

[50] U. Boesenberg, C. G. Ryan, R. Kirkham, D. P. Siddons, M. Alfeld, J. Garrevoet, T. Nez, T. Claussen, T. Kracht, and G. Falkenberg, *Fast x-ray microfluorescence imaging with submicrometer-resolution integrating a Maia detector at beamline P06 at PETRAIII*, J. Synchrotron Radiat. **23**, 1550 (2016).

[51] V. A. Sol, E. Papillon, M. Cotte, P. Walter, and J. Susini, *A multiplatform code for the analysis of energy-dispersive x-ray fluorescence spectra*, Spectrochim. Acta B **62**, 63 (2007).

[52] T. Schoonjans, A. Brunetti, B. Golosio, M. Sanchez del Rio, V. A. Sol, C. Ferrero, and L. Vincze, *The XRAYLIB library for x-ray matter interactions. Recent developments*, Spectrochim. Acta B **66**, 776 (2011).

[53] P. T. Boggs and J. E. Rogers, *Orthogonal distance regression*, NISTIR **89**, 1 (1989).

[54] B. B. Avants, N. J. Tustison, G. Song, P. A. Cook, A. Klein, and J. C. Gee, *A reproducible evaluation of ants similarity metric performance in brain image registration*, NeuroImage **54**, 2033 (2011).

[55] Y. Gossuin, A. Roch, R. N. Muller, P. Gillis, and F. Lo Bue, *Anomalous nuclear magnetic relaxation of aqueous solutions of ferritin: An unprecedented first-order mechanism*, Magn. Reson. Med. **48**, 959 (2002).

[56] I. Arganda-Carreras, V. Kaynig, C. Rueden, K. W. Eliceiri, J. Schindelin, A. Cardona, and H. Sebastian Seung, *Trainable Weka Segmentation: A machine learning tool for microscopy pixel classification*, Bioinformatics **33**, 2424 (2017).

[57] J. Schindelin, I. Arganda-Carreras, E. Frise, V. Kaynig, M. Longair, T. Pietzsch, S. Preibisch, C. Rueden, S. Saalfeld, B. Schmid, J.-Y. Tinevez, D. J. White, V. Hartenstein, K. Eliceiri, P. Tomancak, and A. Cardona, *FIJI: An open-source platform for biological-image analysis*, Nat. Methods **9**, 676 (2012).

[58] A. Deistung, A. Schäfer, F. Schweser, U. Biedermann, R. Turner, and J. R. Reichenbach, *Toward in vivo histology: A comparison of quantitative susceptibility mapping (QSM) with magnitude-, phase-, and R_2*-imaging at ultra-high magnetic field strength*, NeuroImage **65**, 299 (2013).

[59] C. L. Tardif, A. Schäfer, R. Trampel, A. Villringer, R. Turner, and P.-L. Bazin, *Open Science CBS Neuroimaging*

Repository: Sharing ultra-high-field MR images of the brain, NeuroImage **124**, 1143 (2016).

[60] J. W. Sidabras, J. Duan, M. Winkler, T. Happe, R. Hussein, A. Zouni, D. Suter, A. Schnegg, W. Lubitz, and E. J. Reijerse, *Extending electron paramagnetic resonance to nanoliter volume protein single crystals using a self-resonant microhelix*, Sci. Adv. **5**, eaay1394 (2019).

[61] H. C. Davis, P. Ramesh, A. Bhatnagar, A. Lee-Gosselin, J. F. Barry, D. R. Glenn, R. L. Walsworth, and M. G. Shapiro, *Mapping the microscale origins of magnetic resonance image contrast with subcellular diamond magnetometry*, Nat. Commun. **9**, 131 (2018).

[62] H. Toida, K. Sakai, T. F. Teshima, M. Hori, K. Kakuyanagi, Y. O. Imran Mahboob, and S. Saito, *Magnetometry of neurons using a superconducting qubit*, Commun. Phys. **6**, 19 (2023).

[63] L. Zecca, C. Bellei, P. Costi, A. Albertini, E. Monzani, L. Casella, M. Gallorini, L. Bergamaschi, A. Moscatelli, N. J. Turro, M. Eisner, P. R. Crippa, S. Ito, K. Wakamatsu, W. D. Bush, W. C. Ward, J. D. Simon, and F. A. Zucca, *New melanic pigments in the human brain that accumulate in aging and block environmental toxic metals*, Proc. Natl. Acad. Sci. U.S.A. **105**, 17567 (2008).

[64] H.-G. Shin, J. Lee, Y. H. Yun, S. H. Yoo, J. Jang, S.-H. Oh, Y. Nam, S. Jung, S. Kim, M. Fukunaga, W. Kim, H. J. Choi, and J. Lee, *χ-separation: Magnetic susceptibility source separation toward iron and myelin mapping in the brain*, NeuroImage **240**, 118371 (2021).

[65] C. Stüber, M. Morawski, A. Schäfer, C. Labadie, M. Wähnert, C. Leuze, M. Streicher, N. Barapatre, K. Reimann, S. Geyer, D. Spemann, and R. Turner, *Myelin and iron concentration in the human brain: A quantitative study of MRI contrast*, NeuroImage **93**, 95 (2014).

[66] H. Rusch, M. Brammerloh, J. Stieler, M. Sonntag, S. Mohammadi, N. Weiskopf, T. Arendt, E. Kirilina, and M. Morawski, *Finding the best clearing approach—Towards 3D wide-scale multimodal imaging of aged human brain tissue*, NeuroImage **247**, 118832 (2022).

[67] E. Kirilina, S. Helbling, M. Morawski, K. Pine, K. Reimann, S. Jankuhn, J. Dinse, A. Deistung, J. R. Reichenbach, R. Trampel, S. Geyer, L. Müller, N. Jakubowski, T. Arendt, P.-L. Bazin, and N. Weiskopf, *Superficial white matter imaging: Contrast mechanisms and whole-brain in vivo mapping*, Sci. Adv. **6** (2020).

[68] R. Trampel, P.-L. Bazin, K. Pine, and N. Weiskopf, *In-vivo magnetic resonance imaging (MRI) of laminae in the human cortex*, NeuroImage **197**, 707 (2019).

[69] T. Leutritz, M. Seif, G. Helms, R. S. Samson, A. Curt, P. Freund, and N. Weiskopf, *Multiparameter mapping of relaxation (R1, R2*), proton density and magnetization transfer saturation at 3 T: A multicenter dual-vendor reproducibility and repeatability study*, Hum. Brain Mapp. **41**, 4232 (2020).

[70] M. Morawski, C. Meinecke, T. Reinert, A. Dörffel, P. Riederer, T. Arendt, and T. Butz, *Determination of trace elements in the human substantia nigra*, Nucl. Instrum. Methods Phys. Res., Sect. B **231**, 224 (2005).

[71] T. Reinert, D. Spemann, M. Morawski, and T. Arendt, *Quantitative trace element analysis with sub-micron lateral resolution*, Nucl. Instrum. Methods Phys. Res., Sect. B **249**, 734 (2006).

[72] T. Reinert, A. Fiedler, M. Morawski, and T. Arendt, *High resolution quantitative element mapping of neuromelanin-containing neurons*, Nucl. Instrum. Methods Phys. Res., Sect. B **260**, 227 (2007).